

Journal Pre-proofs

Prograde and retrograde metasomatic reactions in mineralised magnesium-silicate skarn in the Cu-Au Ertsberg East Skarn System, Ertsberg, Papua Province, Indonesia

Melanie J. Sieber, Frank J. Brink, Clyde Leys, Penelope L. King, Richard W. Henley

PII: S0169-1368(20)30427-3
DOI: <https://doi.org/10.1016/j.oregeorev.2020.103697>
Reference: OREGEO 103697

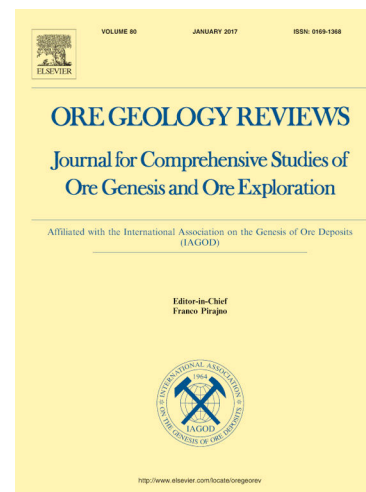
To appear in: *Ore Geology Reviews*

Received Date: 30 April 2020
Revised Date: 22 July 2020
Accepted Date: 26 July 2020

Please cite this article as: M.J. Sieber, F.J. Brink, C. Leys, P.L. King, R.W. Henley, Prograde and retrograde metasomatic reactions in mineralised magnesium-silicate skarn in the Cu-Au Ertsberg East Skarn System, Ertsberg, Papua Province, Indonesia, *Ore Geology Reviews* (2020), doi: <https://doi.org/10.1016/j.oregeorev.2020.103697>

This is a PDF file of an article that has undergone enhancements after acceptance, such as the addition of a cover page and metadata, and formatting for readability, but it is not yet the definitive version of record. This version will undergo additional copyediting, typesetting and review before it is published in its final form, but we are providing this version to give early visibility of the article. Please note that, during the production process, errors may be discovered which could affect the content, and all legal disclaimers that apply to the journal pertain.

© 2020 Published by Elsevier B.V.



1 **Prograde and retrograde metasomatic reactions in mineralised magnesium-silicate**
2 **skarn in the Cu-Au Ertsberg East Skarn System, Ertsberg, Papua Province, Indonesia**

3 ^{1,2*}Sieber, Melanie J., ³Brink, Frank J., ⁴Leys, Clyde, ¹King, Penelope L. and ⁵Henley, Richard
4 W.

5 1. Research School of Earth Science, The Australian National University, Canberra ACT 0200,
6 Australia

7 2. Present address: University of Potsdam, Institute for Mineralogy, Potsdam, Germany

8 3. Centre for Advanced Microscopy, The Australian National University, Canberra ACT 0200,
9 Australia

10 4. P.T. Freeport Indonesia, Tembagapura, Papua, Indonesia

11 5. Department of Applied Mathematics, Research School of Physics, The Australian National
12 University, Canberra ACT 0200, Australia

13 * Corresponding author, melanie.sieber@uni-potsdam.de, +49 331 977 5671
14

15 **Abstract**

16 The 2.7-2.9 Ma Ertsberg East Skarn System (EESS) is a world-class Cu-Au skarn that formed within
17 and adjacent to an intrusion within a paleodepth of 0.5 km and > 2.5 km. Its economic mineralisation
18 developed by sustained reaction of magmatic fluid with contact metamorphosed siliciclastic and
19 carbonate rocks at the margin of the adjacent Ertsberg quartz monzodiorite intrusion. Based on high-
20 resolution mineral mapping, chemical analysis and thermodynamic calculations, the multistage
21 formation processes of the exoskarn components of the EEES are examined in the context of
22 changing pressure, temperature, fluid composition and fluid phase. We show that contact
23 metamorphism of dolomitic sediments occurred at 51 ± 5 MPa, between 700 °C and 800 °C and in the
24 presence of a H₂O-CO₂-fluid containing ~10 to ~70 mol% CO₂. This prograde metamorphism formed
25 a forsterite + diopside + calcite + phlogopite + spinel assemblage. Such forsterite-dominated skarns
26 account for ~55 vol.% of the EEES exoskarns. Rare pargasite (previously unrecognized in this
27 deposit) formed locally in the metamorphosed carbonate sequence where the protolith was composed
28 of supratidal evaporites with dolomitic carbonate and interlayered calc-silicate rocks. The subsequent
29 flux of a lower pressure magmatic *gas* containing SO_{2(g)} caused sulphate metasomatism. This high
30 temperature gas alteration of the metamorphic assemblage also caused skarn Cu-Fe-sulphide
31 mineralisation. The influx of a SO₂ gas through fracture permeability occurred at a temperature
32 between ~600 and 700 °C and caused calcite to be replaced by anhydrite, with the coupled release of
33 H₂S_(g). This *in-situ* release of H₂S_(g) scavenged trace Cu from the gas phase to deposit Cu-Fe-
34 sulphides, which make the economic value of the distinct. We demonstrate that the formation of

35 metal sulphides within forsterite skarns of the Ertsberg East Skarn System required a minimum flux of
36 $\sim 1,050$ Mt $\text{SO}_{2(g)}$ and show that volcanic degassing may have occurred over a time span of $\sim 3,900$
37 years. As the system waned, the ambient fluid resulted in partial retrograde serpentinization of olivine
38 and diopside without carbonation, and at temperatures sufficiently high to preserve anhydrite.

39 **Keywords**

40 Porphyry Cu-Au deposit

41 Magnesium silicate skarn

42 Pargasite

43 Gas-solid reaction

44 Sulphate metasomatism

45

46 **1 Introduction**

47 The Ertsberg East Skarn System (EESS), a world-class exo- and endoskarn-hosted copper and gold
48 deposit is located near to the giant Grasberg porphyry Cu-Au deposit in eastern Indonesia (Fig. 1)
49 (Leys et al., 2012). Mineralisation in the EESS is superimposed on the northern margin of the
50 Ertsberg intrusion as well as on a large mass of siliciclastic and carbonate units of the Cenozoic New
51 Guinea Limestone Group that were metamorphosed to calcium-magnesium silicate skarns during
52 emplacement of that stock (Kyle et al., 2014). Such intrusion-related skarn systems have
53 complex mineral associations (Einaudi and Burt, 1982; Pirajno, 2013) due to primary
54 geochemical variations across their host stratigraphy and the extent of metasomatic alteration. Contact
55 metamorphism of the New Guinea Limestone Group produced Ca-rich garnet-diopside silicate rocks
56 and forsterite marbles through decarbonation and dehydration reactions (Turner, 1981). These
57 metamorphic assemblages have been comprehensively described by Gandler (2006) emphasizing
58 how the variability of skarn mineralogy is related to both protolith composition and temperature
59 via proximity to the intrusion contact. Subsequent magmatic fluid flux along fracture arrays
60 through the contact metamorphosed carbonate sequence led to skarn mineralisation (Gandler,
61 2006; Henley and Seward, 2018; Meinert et al., 1997). Fluid inclusion and sulphur isotope
62 data imply that the skarn mineralisation developed at temperatures above ~ 600 °C (Baline, 2007;
63 Gibbins, 2006; Harrison, 1999; Mertig, 1995; Mertig et al., 1994).

64 In the EESS, Henley et al. (2017) showed that the mineralised calc-silicate mineral
65 assemblages dominated by garnet (andradite and grossular), anorthite and anhydrite formed through
66 poly-diffusive gas-solid reactions as a consequence of the flux of magmatic gas through
67 calcareous marble units. However, new data provided from extensive proprietary drilling reveal that
68 such garnet-bearing skarns comprise less than 5 % rock volume (vol.%) of the total mineralised

69 exoskarn skarn bodies in the EESS. Thus, an understanding of the fluid-rock metasomatic reactions
70 at a scale of km³ requires analysis of the much more abundant, mineralised anhydrite-magnetite-
71 forsterite skarn. These Mg-rich mineralised skarns make up ~55 vol.% of the total ~0.93 km³ volume
72 of the EESS exoskarns and their petrogenesis is the focus of this study. The remaining volume
73 (~0.36 km³) of mineralised exoskarn assemblages is comprised of other co-genetic assemblages
74 including magnetite-rich and hornfels skarns. The mass of EESS metasomatised and mineralised
75 sedimentary rock is at least 2,600 Mt (the estimated tonnage of EESS exoskarns).

76 In this paper, we provide new geochemical and mineralogical data for the dominant Mg-rich silicate
77 skarn assemblages enabling a comprehensive model to be developed for the succession of fluid-rock
78 interaction processes that occurred from contact metamorphism, through fluid release from high-level
79 intrusions to subsequent retrograde reactions. The samples analysed here are exoskarns meaning
80 contact metamorphic skarns outboard of the associated igneous intrusion. However, we have
81 otherwise not adopted any of the empirical classification schemes that are used in lithological
82 mapping to distinguish mineralisation types through individual deposits (Meinert et al., 2005).
83 Rather we have focussed on distinguishing first-order variations in overall chemistry (Ca-rich vs.
84 Mg-rich), that are related to protolith composition, and consequent, second order variations in
85 mineralogy (Ca-silicate skarns vs. Mg-silicate skarns). We have developed a new bulk geochemical
86 model for the large-scale metasomatic processes that converted contact metamorphic skarn
87 assemblages to oxidised sulfate-rich mineralised rock with CuFe-sulphides as a by-product.
88 Understanding of skarn formation and mineralisation extends beyond the economically significant
89 skarns at Ertsberg and elsewhere because the high temperature fluid-rock reaction processes discussed
90 here are also applicable to the interpretation of processes beneath modern active volcanoes, such
91 as Vesuvius (Italy) and Lascar (Chile), where mineralised skarn ejecta are found (Fulignati et al.,
92 2001; Matthews et al., 1996).

93 **2 Geological setting**

94 The formation of the Ertsberg East Skarn System (EESS) is a consequence of emplacement of the 2.9
95 to 2.7 Ma Ertsberg intrusion into regionally extensive Cenozoic New Guinea Limestone Group
96 sediments (Fig. 1) (Kyle et al., 2014). The Ertsberg intrusion comprises a quartz monzonite to
97 quartz monzodiorite stock that was emplaced at ≤ 2 km depth into the Cenozoic and older sedimentary
98 formations (McMahon, 1994). The New Guinea Limestone Group is comprised of mixed
99 siliciclastic and carbonate units, interpreted to have been deposited on a shallow marine shelf. One of
100 the principal stratigraphic units that developed into mineralised skarns within the New Guinea
101 Limestone Group is the folded, ~0.3 km thick Paleocene Waripi Formation comprised of
102 dolostone, siltstone, dolomitic to sandy limestone, calcareous sandstone, calcareous mudstone, sandy
103 dolomite and sandstone (Gandler, 2006; Meinert et al., 1997). Towards the top of the Waripi
104 Formation the abundance and thickness of sandstone increases and anhydrite nodules are present as

105 a minor component (Gandler, 2006). The Waripi Formation is overlain by Eocene Faumai
106 Formation massive limestones and sandstones (Gandler, 2006; Meinert et al., 1997).

107 For this study, a suite of skarn samples was provided by PT Freeport Indonesia from a single
108 underground drill hole (TE06-24) through the Deep Mill Level Zone of the EESS. Based on
109 reconnaissance analyses, two samples (CS1 and FM1) were selected that best exhibited distinct
110 compositional variations related to the sedimentary precursor, sulphide-sulfate mineralisation and
111 retrograde alteration. CS1 and FM1 present samples of altered Waripi Formation at a depth of
112 ~1,600 m below the present surface, and located 9.5 m (CS1) and 98.7 m (FM1) from the
113 Ertsberg intrusion contact (Fig. 1b and c). Part of sample CS1 (TE06-24: 270.6 m) was described as
114 an altered and mineralised calc-silicate skarn (Henley et al., 2017). In this study, we
115 investigated the contiguous lower part of that sample that has a contrasting Mg-silicate
116 assemblage and the contact zone between the calc-silicate and the Mg-silicate assemblages. New
117 data for phase relations in this distinct assemblage is provided as a basis for further refining
118 the understanding of metasomatic processes during subsequent mineralisation. Based on a second
119 sample (FM1), new analytical data is also provided for mineral assemblages in the forsterite marble
120 sequence that makes up ~55 vol.% of the exoskarn component of the EESS deposit and which was
121 subsequently altered to a Mg-silicate + anhydrite assemblage with Cu-Fe-sulphides (sample FM1;
122 TE06-24: 359.9 m).

123 **3 Analytical methods and thermodynamic calculation**

124 **3.1 Analytical methods**

125 Polished thick sections of CS1 and FM1 were prepared using dry cutting and water-free polishing
126 paste. Mineral phases were identified using a JEOL 6610A scanning electron microscope (SEM)
127 equipped with an Energy Dispersive spectroscopy (EDS) system at the Research School of Earth
128 Sciences, Australian National University (ANU). Selected mineral phases were quantitatively
129 analysed using a JEOL JXA-8530F Plus Microprobe equipped with 5 wavelength dispersive
130 spectrometers (WDS) at the Centre for Advance Microscopy (CAM), ANU. We used a 50 nA probe
131 current and an accelerating voltage of 8 kV to improve spatial resolution. The system was calibrated
132 against well-characterised standards including periclase (Mg), diopside (Ca), sanidine (Si, K),
133 hematite (Fe), albite (Al), CaF₂ (F), albite (Na), rutile (Ti) and chromite (Cr). Almandine, pyrope and
134 chlorite were used as secondary standards to monitor measurement performance. The FEI Quanta
135 650F “TMQEMSCAN” (Quantitative Evaluation of Minerals) at CAM was used to collect EDS-Field
136 Emission (FE)-SEM maps for visualising the mineral distribution. Mapping was performed using
137 10 nA probe current, 15 kV accelerating voltage, a count rate of approximately 420,000 counts per
138 second, 3,000 counts/pixel and a step size of 9.9 μm. TMQEMSCAN uses a EDS library to
139 automatically recognise mineral phases. In addition, TMQEMSCAN mineral mapping was calibrated

140 by independent SEM spot analyses allowing measured mineral compositions to be correlated with
141 mineral phases. Mineral proportions within a given field of interest were computed with the
142 TMQEMSCAN software.

143 3.2 Thermodynamic modelling

144 For the purposes of thermodynamic modelling and determination of the temperature condition and the
145 CO₂-H₂O fluid composition during contact metamorphism, the bulk rock compositions were
146 constrained from the phase abundances established in the TMQEMSCAN maps and the composition of
147 mineral components (Table 1). The bulk rock compositions were calculated considering the
148 proportion and composition of mineral phases with abundances >1 area% in the TMQEMSCAN map.
149 Using the bulk compositions (listed in Table 1) to reconstruct the composition of the sedimentary
150 precursor assumes negligible chemical gains or losses, except for variations of the volatile
151 components, during prograde and retrograde reactions (Stage 1, 2 and 3). This assumption is
152 reasonably well sustained for sample FM1, because the reconstructed bulk composition of FM1 is in
153 accordance with unmetamorphosed and unaltered dolomitic sandstone and limestone of the Waripi
154 Formation (Gandler, 2006) (Fig. 2). Accordingly, the bulk composition of FM1 implies a sandy
155 dolostone as sedimentary precursor. However, the Mg-rich-silicate and the contact-zones of sample
156 CS1 (hereafter referred to as CS1-Mg-rich-silicate and CS1-contact-zone respectively) are enriched
157 in e.g. Na, K, Al and Mg+Fe compared to unmetamorphosed rocks of the Waripi Formation reported
158 by Gandler (2006) (Fig. 2 and Table 1 in the supplementary information).

159 Isobaric temperature- $X_{\text{CO}_2}^{\text{fluid}}$ pseudosections were computed with the Perple_X thermodynamic
160 software package (version 6.8.4; Connolly (2009)) using the CORK equation of state for the fluid and
161 thermodynamic data from Holland and Powell (1991); Holland and Powell (1998, 2011). $X_{\text{CO}_2}^{\text{fluid}}$ is
162 defined as the mole fraction of CO₂ in a CO₂-H₂O-bearing fluid. Solid solution models employed in
163 the calculations include: biotite, chlorite, chloritoid, cordierite, garnet, melt, mica, orthopyroxene,
164 staurolite after White et al. (2014); sapphire after Wheller and Powell (2014); feldspar after Fuhrman
165 and Lindsley (1988); carbonate after Holland and Powell (2003); clinopyroxene and olivine after
166 Holland and Powell (1998); spinel after White et al. (2002) and clino- and orthoamphibole after
167 Diener and Powell (2012). The volatile-free, bulk compositions of the Mg-silicate skarns were
168 modelled in the SiO₂-Al₂O₃-FeO-MgO-CaO-Na₂O-K₂O-system and assume connected porosity with a
169 single-phase CO₂-H₂O fluid at 51 MPa. Note, that minor amounts of Na₂O (~4 ppm) in the bulk
170 composition of FM1 were omitted in the thermodynamic modelling. For assumptions and reasoning
171 of this pressure (51 MPa) the reader is referred to section 5.1.1.

172 4 Mineral chemistry

173 Below, we provide a petrographic description of two Mg-silicate skarn samples (CS1 and FM1) from
174 the East Ertberg Skarn System based on high resolution TMQEMSCAN maps and EPMA mineral

175 analysis (Table 1).

176 4.1 Sample FM1

177 The section of sample FM1 consists of mostly anhydrite (76 area%), significant serpentine (15
178 area%), some magnetite and forsterite and traces of phlogopite and sulphides (Fig. 3; Table 1).
179 This assemblage has neither diopside nor brucite although both phases occur in adjacent parts of the
180 rock sequence indicating a primary variability of Ca/Mg ratio in the sediment or variations in the fluid
181 composition. The TMQEMSCAN maps of FM1 show an equigranular texture of anhydrite and
182 partially serpentinized forsterite (Mg#~95.5) with interstitial and idioblastic grains of phlogopite (Fig.
183 3a-b). Phlogopite crystals are up to ~1 mm long, homogeneous with Mg#~92.3 and rarely occur as
184 inclusions in olivine (Fig. 3c).

185 4.2 Sample CS1

186 Sample CS1 shows a contact between an upper calc-silicate unit and a lower, Mg-rich unit marking
187 compositional variations in the sedimentary precursor and subsequent alteration reactions (Fig. 4a).
188 The contact zone between the upper *CS1-calc-silicate* (orange-brown) and lower *CS1-Mg-rich-*
189 *silicate* (green) is well-defined in the hand specimen by a change in colour (Fig. 4a). The *CS1-*
190 *calc-silicate* is the subject of a previous study and it contains garnet (andradite and grossular),
191 anorthite, anhydrite, clinopyroxene, epidote, chalcocopyrite, orthoclase, calcite, apatite and minor
192 quartz (Henley et al., 2017).

193 4.2.1 *CS1-contact-zone*

194 The contact-zone between the *CS1-calc-silicate* and *CS1-Mg-rich-silicate* is ~1 cm wide and light
195 green. The upper part of the contact zone, *CS1-upper-contact*, is dominated by diopside (80 area%),
196 with much less phlogopite (12 area%) and pargasite, minor anhydrite, and trace spinel, garnet and
197 bornite (each ≤ 0.1 area%; Table 1). The lower part of the contact zone, *CS1-lower-contact*, is
198 dominated by phlogopite (54 area%) and contains lesser pargasite (22 area%) and diopside (16
199 area%), with minor Al-spinel and anhydrite and trace bornite, Cr-spinel, hematite, magnetite,
200 olivine, serpentine and garnet (each ≤ 0.6 area%; Table 1). The distinct change in mineral assemblage
201 and mode within the contact zone is interpreted to reflect compositional variation in the sedimentary
202 precursor together with different degrees of metasomatic overprint (see 5. *Discussion*).

203 The upper contact zone contains tabular phlogopite enclosed by irregularly-shaped diopside. The
204 grain size and abundance of phlogopite increases towards the Mg-rich silicate part of sample CS1
205 (Fig. 4b and 5a) and phlogopite crystals show an irregular habit in the lower contact zone (Fig. 5a-b).
206 Throughout the entire contact zone, spinel has irregular grain boundaries and is enclosed in phlogopite
207 implying partial replacement of spinel by phlogopite. Poikiloblasts of medium-grained Na-amphibole
208 (pargasite) occur predominantly in axial plane cleavage (subparallel to the stratigraphic contact

209 between the calc-silicate and the Mg-rich silicate rocks) that cuts across an anhydritic lamina within
 210 the contact zone (Fig. 4b). This lamina may be a primary feature of the evaporitic protolith.
 211 Pargasite also occurs within the *CSI-Mg-rich-silicate* (Fig. 5c). Pargasite grains contain inclusions of
 212 phlogopite and diopside (Fig. 5b-c). Furthermore, pargasite grains are homogeneous and have, in
 213 contrast to phlogopite crystals, a more consistent composition across the contact zone (Mg#=82.5-
 214 83.5). The abundance of diopside crystals decreases across the contact zone from the *CSI-calc-*
 215 *silicate* to the *CSI-Mg-rich-silicate*. Diopside grains in the contact zone are inhomogeneous and
 216 contain at least three distinct zones identified by their different contrast intensities in BSE-images
 217 (Fig. 6). Within a single diopside grain, the composition varies from Fe- and Al-rich with 100 * molar
 218 $Mg/(Mg+Fe)=Mg\#$ of 80.8 ± 1.6 (2σ) and 0.22 ± 0.01 apfu Al (apfu = atoms per formula unit; here for
 219 6 oxygens), to an intermediate composition with Mg# of 93.2 ± 2.2 and Al=0.08 apfu to a Fe- and Al-
 220 poor composition showing Mg# of 98.8 ± 1.4 and Al of $\leq 0.1\pm 0.1$ apfu (Fig. 6). Fe and Al-rich
 221 diopside grains are low in silica (Si= 1.8 ± 0.01 apfu) and may contain some water (~0.7 wt.%) as
 222 implied by systematically low analytical totals from electron microprobe analyses.

223 Individual phlogopite grains are homogeneous in the contact zone, but the Mg# of phlogopite crystals
 224 changes gradually across the contact. In *CSI-lower-contact*, phlogopite crystals are richer in Mg
 225 (Mg#~92) relative to phlogopite grains close to *CSI-calc-silicate* (Mg#~90). Grains of phlogopite
 226 commonly surround Al-spinel crystals ($Mg_{0.76}Fe_{0.26}^{2+}Fe_{0.06}^{3+}Al_{1.94}O_4$; Mg#=74.5) and contain small
 227 amounts of Na (~0.03 apfu; for 11 oxygens).

228 4.2.2 *CSI-Mg-rich-silicate*

229 The *CSI-Mg-rich-silicate* (below the contact) is dominated by pargasite (42 area%), with significant
 230 forsterite (25 area%), some diopside, serpentine and phlogopite, minor anhydrite and trace (≤ 0.3
 231 wt.%) bornite, hematite, Al-spinel, magnetite, chlorite and spadaite ($MgSiO_2(OH)_2 * x H_2O$) (Fig. 5,
 232 Table 1). Forsterite, diopside and phlogopite are xenomorphic (Fig. 5b-c). Serpentine and
 233 magnetite replace forsterite (and diopside) along veinlets that are texturally unrelated to pargasite (at
 234 the bottom of Fig. 5a). Phlogopite crystals in the *CSI-Mg-rich-silicate* have high Mg# of 92 to 93 and
 235 contain some Ti ($TiO_2=0.2$ wt.%); they are homogeneous and may surround Al-spinel in places.
 236 Pargasite grains are homogeneous and have Mg# of ~83 (ranging from 82.5 to 84.2). Diopside
 237 crystals show the patchy, irregular composition seen in diopside crystals within the contact zone.
 238 Forsterite crystals display Mg zoning with highest Mg# of 96.9 in the cores (ranging from 93.4 to
 239 98.3) and Fe-rich rims (Mg# median is 91.8; Mg# ranges from 90.9 to 95.4). Serpentine has a
 240 median Mg# of 96.7 (ranging from 95.9 to 97.8) and contain some Al when replacing diopside
 241 (Al<<0.1 apfu for 7 oxygens). Clinocllore is fibrous, fine-grained, Cr-free and has Mg# of ~95.6 and
 242 spadaite has Mg#~90.4. Fine-grained and euhedral magnetite grains within veinlets are likely formed
 243 as a result of forsterite hydration.

244 4.3 Sulphide minerals in CS1 and FM1

245 Although Cu-Fe-sulphide grains constitute <1 area% of the mineral maps (Fig. 3, 4 and 5) for the
246 studied samples (CS1 and FM1), the copper content that they contribute to the rock is responsible for
247 the economic value of the EESS. Since the unmetamorphosed protolith (sandy dolostone - limestone)
248 does not contain any copper, the presence of Cu-Fe-sulphides is testimony to the pervasive, post-
249 contact metamorphism flux of a fluid phase containing sulphur plus these metals. Cu-Fe-sulphide
250 grains are texturally associated with anhydrite (Fig. 4c). Individual Cu-Fe-sulphide grains are either
251 bornite-chalcocite solid solutions or Zn-bearing covellite (Fig. 7). Within a single sulphide grain, the
252 composition ranges between bornite and chalcocite. The compositional variability within individual
253 sulphide grains is evident in BSE-images (Fig. 7c, d) and likely reflect exsolution from Independent
254 Solid Solution (ISS) on lowering temperature below about 700 °C (Fig. 7e) (Kullerud et al.,
255 1969; Yund and Kullerud, 1966).

256 5 Discussion

257 Here we describe the evolution of the Mg-silicate skarns (CS1 and FM1) from contact metamorphism
258 of carbonate-rich sediments (Stage 1), subsequent skarn mineralisation by their reaction with a flux of
259 magmatic gas (Stage 2) and finally retrograde, hydrothermal alteration (Stage 3). The mineral
260 chemistry data for the Mg-rich silicate skarns provide the basis for determining the pressure and
261 temperature conditions (contact metamorphism – Stage 1) under which the Mg-silicates formed in the
262 Ertsberg hydrothermal system. These conditions may then be related to pressure and temperature
263 conditions during fluid flow in the subsequent stages (Stage 2 and 3) as is discussed below.

264 5.1 Stage 1: Contact metamorphism

265 In the following we argue that contact metamorphism occurred at a pressure of 51 ± 5 MPa and peak
266 metamorphic temperature of 750 ± 50 °C in the presence of a CO₂-H₂O-fluid containing between ~10
267 to ~70 mol% CO₂. First, constraints on the pressure during contact metamorphism will be provided.
268 Then, the mineral assemblages formed during contact metamorphism, the metamorphic temperature
269 and fluid composition are considered based on thermodynamic modelling.

270 5.1.1 Constraints of the pressure during contact metamorphism

271 There are two methods to constrain the confining pressure at the paleodepth of each sample. First,
272 data from Wafforn et al. (2018) and Wafforn (2017) using U-Pb zircon and garnet and U-Th/He
273 apatite ages from vertical profiling in the Grasberg deposit indicates the maximum difference in
274 elevation between the present-day surface and paleo-surface of ~1 km. Second, lake sediments that
275 are preserved immediately above the older Grasberg porphyry copper deposit (only 3 km away)
276 indicate the elevation of the paleo-surface 300,000 years before the Ertsberg deposits formed. These
277 lake sediments outcrop at 4.2 km a.s.l. (above sea level) so that we may conservatively estimate that

278 the paleo-surface was at about 4.5 km a.s.l. (Fig. 1d). Considering subsidence and compaction of the
279 lake beds at Grasberg, volcanic topography, and the low amplitude of subsequent folding and faulting
280 during uplift of the region provides an estimated uncertainty of ~ 0.2 km. This suggests that the
281 maximum difference between the present-day surface and paleo-surface is ~ 0.5 km (Fig. 1d). Since
282 the investigated drillhole samples were obtained from a depth of ~ 1.6 km, the paleodepth of the
283 sample is about 2.1 km below surface (Fig. 1d), equal to a lithostatic pressure of 51 ± 5 MPa. This
284 pressure estimate assumes densities for quartz- and carbonate-rich sediments of $2,648 \text{ kgm}^{-3}$ and $2,710$
285 kgm^{-3} , respectively, and average porosities for sandstones of 12 vol.% and for limestones of 4.3
286 vol.% after Barrell (1914). Within uncertainty, this pressure (51 ± 5 MPa) correlates well with the
287 pressure of 49 ± 10 MPa estimated by Henley et al. (2017) from the *CSI-calc-silicate* and
288 thermodynamic modelling.

289 5.1.2 Contact metamorphism

290 The thermal decomposition of sedimentary carbonate rocks releases significant amounts of CO_2 and
291 H_2O . In order to model the mineral variability caused by different fluid compositions over a range of
292 temperature, isobaric $T\text{-}X_{\text{CO}_2}^{\text{fluid}}$ pseudosections were calculated, assuming that the system was
293 saturated by an interconnected $\text{CO}_2\text{-H}_2\text{O}$ fluid. CO_2 and H_2O were considered in the modelling,
294 because these are the dominant fluids released during devolatilization of carbonaceous sediments
295 such that other volatile species can be neglected in the contact metamorphic stage. Pseudosection
296 main stability fields are shown in Figure 8 and they were modelled at 51 MPa using the
297 reconstructed, volatile-free, bulk composition in respect to SiO_2 , Al_2O_3 , MgO , FeO , CaO , Na_2O and
298 K_2O (Table 1). The modelled, isobaric $P\text{-}X_{\text{CO}_2}^{\text{fluid}}$ pseudosection for sample FM1 shows that an
299 assemblage of calcite + forsterite + diopside + phlogopite + spinel is stable over a wide range of
300 $\text{CO}_2\text{-H}_2\text{O}$ fluid composition and a temperature between ~ 550 and ~ 760 °C (Fig. 8b). Within this
301 stability field, the abundance and composition of mineral phases (Table 2) are marginally sensitive to
302 changes in temperature and fluid composition. The assemblage of calcite + forsterite + diopside +
303 phlogopite + spinel is restricted by the absence of phlogopite for temperatures above ~ 800 °C. At T
304 $\lesssim 550$ °C, spinel is absent and chlorite is stable (Fig. 8). We interpret this assemblage of calcite +
305 forsterite + diopside + phlogopite + spinel as the contact metamorphic paragenesis. Forsterite +
306 diopside + carbonate (calcite + dolomite) record decarbonation reactions in siliceous, dolomitic
307 marbles (e.g. Bucher-Nurminen (1982); Bucher and Grapes (2011); Skippen (1974)).
308 Calcite was efficiently replaced by anhydrite in the reaction of a high temperature fluid with the
309 contact metamorphic assemblages (see section 5.2 *Stage 2: Mineralisation and alteration*). The
310 granular texture of FM1, and the idiomorphic shape of phlogopite crystals and occurrence as
311 inclusions in forsterite grains of sample FM1 (Fig. 3c), imply that phlogopite and forsterite
312 grains formed together or phlogopite formed slightly earlier. Interpretation of the modelled, high

313 pressure and temperature phase relations is limited to two assumptions. Firstly, local mineral-
314 fluid equilibrium along the flow path of the fluid is assumed. Secondly, the modeling considers a
315 closed system. The latter assumption may not be fully achieved, since Stage 2 fluid flux partially
316 modified the bulk chemistry particularly in respect of fluid mobile elements such as S, Fe, Na and
317 K and metals such as Cu. However, the reconstructed bulk rock composition of sample FM1
318 correlates reasonably to unmetamorphosed parts of the Waripi Formation after Gandler (2006) for major
319 elements such as Si, Mg+Fe and Ca (Fig. 2 and Table 1 in the supplementary information). The
320 contact metamorphic assemblage described here is stable over a wider range of CO₂-H₂O-fluid
321 composition up to a maximum temperature of 750 ± 50 °C (Fig. 8). Thus, we consider this
322 temperature as the peak metamorphic temperature at a pressure of 51 ± 5 MPa. The obtained peak-
323 metamorphic temperature is equal to the temperature during contact metamorphism reported by
324 Henley et al. (2017) for the *CS1-calc-silicate* from the same drill core.

325 At 750 ± 50 °C and 51 ± 5 MPa, an equilibrium mineralogy of forsterite, pargasite, diopside,
326 phlogopite and some calcite and spinel could be modelled for the reconstructed bulk composition of
327 the *CS1-Mg-rich-silicate* (Fig. 8a). The reconstructed bulk composition of the *CS1-Mg-rich-silicate*
328 and the *CS1-contact-zone* show higher Na, K, Al and Mg+Fe compared to the overall composition of
329 the sedimentary units of the Waripi Formation (Fig. 2 and Table 1 in the supplementary information).
330 The chemical variation is interpreted to reflect small-scale mineralogical variations in the sedimentary
331 precursor in combination with element transport during rock-fluid interaction. The correlation
332 between the modelled peak metamorphic assemblage of forsterite, pargasite, diopside, phlogopite and
333 some calcite (fully replaced by anhydrite during Stage 2) and spinel to the present assemblage indicate
334 minor gains or losses of elements. However phlogopite crystals in the *CS1-contact-zone* are irregular
335 shaped and corroded, and the Mg# of phlogopites gradually increases from the calc-silicate towards
336 the Mg-silicate zone of CS1. This suggests that an alternative interpretation for these systematic
337 changes may be compositional variations within the sediment or related to element transport across
338 the contact zone. Also, in the *CS1-contact-zone* anhydrite (as a replacement of calcite) and associated
339 Cu-Fe-sulphides occur together with minor pargasite (Fig. 4c and 5c). These distinctive Na-rich areas
340 in the *CS1-contact-zone* raise questions about the source of the sodium required for pargasite
341 formation. Pargasite is most likely a prograde metamorphic phase (Stage 1) because it is commonly
342 found in K-Mg-rich laminae indicative of evaporite-rich layers in the metasediments. We rule out
343 pargasite formation during Stage 2 because Na and K concentrations are too low in magmatic fluids
344 (10^{-3} to 10^{-5} mol/kg; Henley and Seward (2018)). Around 2.5 wt% halite (NaCl) and 2 wt%
345 sylvite (KCl) in the sedimentary precursor are sufficient to contribute the amount of Na and K
346 needed to form the observed amount of pargasite and phlogopite in the Mg-silicate CS1. This mass-
347 balance calculation assumes negligible modification of the bulk rock composition and suggests that
348 the carbonate-quartz-kaolinite-halite-sylvite sediment was a minor part of a lagoonal sedimentary

349 sequence. Figure 4c and 4b shows that anhydrite and Cu-Fe-sulphide grains, with some void space,
350 infill a weak axial planar cleavage in the folded pargasite-rich lamellae through the contact zone. This
351 textural relationship further supports the interpretation of pargasite as a Stage 1 contact metamorphic
352 mineral formed in a Na-bearing protolith. The stability of pargasite in the modelled phase diagram
353 (Fig. 8a) demonstrates that pargasite is stable up to peak metamorphic PT-conditions. Pargasite has
354 not been previously reported at Ertsberg, but it has been reported as a prograde phase in
355 metacarbonates (e.g. Proyer et al. (2008); Satish-Kumar et al. (2001); Thu and Enami (2018)) and it
356 may form during metamorphism of sodic evaporite-bearing sequences (Pirajno, 2018; Warren,
357 2016; Zhu et al., 2015). All these observations point towards the formation of pargasite during
358 prograde metamorphism (Stage 1).

359 5.2 Stage 2: Mineralisation and alteration

360 Economic mineralisation within the EESS contact metamorphic skarns is caused by reaction of a high
361 temperature fluid during Stage 2 with the mineral assemblages that developed during Stage 1. First,
362 we provide geologic and geochemical evidence to demonstrate that the fluid in Stage 2 was derived
363 primarily from a magmatic source. Second, we establish the pressure and temperature range during
364 Stage 2 alteration and mineralisation of the contact metamorphosed carbonate sequence and show that
365 the fluid must have behaved as a low-density fluid (gas) in fracture arrays to produce the Cu-rich
366 skarn resources. Third, we discuss the reactions that replaced calcite with anhydrite and deposited
367 Cu-Fe-sulphides through reaction of the contact metamorphic assemblage with a flux of a magmatic
368 gas.

369 5.2.1 Role for magmatic fluids

370 Carbonate grains are (partially to completely) replaced by anhydrite in Stage 2. Some relicts of calcite
371 have been observed in the calc-silicate part of sample CS1 (Henley et al., 2017). Furthermore, powder
372 X-ray diffraction data of altered Waripi Formation drill-core samples located less than ~90 m
373 from sample FM1 indicate the presence of Mg-Fe-Ca-carbonates such as calcite, dolomite, magnesite
374 and siderite. While the Waripi Formation contains some sedimentary anhydrite nodules
375 (Gandler, 2006; Kyle et al., 2014), most anhydrite formed during replacement of
376 contact metamorphosed carbonates in Stage 2. This is indicated by the high abundance of anhydrite
377 in sample FM1 and the textural association of anhydrites and sulphides. Furthermore, sulphur
378 isotopic data for sulphide and anhydrite grains within veins from the Grasberg Intrusive Complex
379 and the EESS reveal component contributions from sulphur-bearing country rocks (e.g. the anhydrite
380 nodules in the New Guinea Limestone Group) and from a deep magma source, whereby the latter
381 becomes more significant over time (Gibbins, 2006). For these reasons, it is necessary to access a
382 larger reservoir of sulphur to form the abundant Stage 2 anhydrite and sulphides found throughout
383 the EESS. This is resolved through oxygen isotope data by recognizing that the H₂O in the Stage

384 2 mineralising fluid was primarily derived from an underlying magmatic complex (Gibbins, 2006)
 385 as might be anticipated because of its porphyry copper system origin (Henley and Seward, 2018).

386 The Ertsberg East Skarn System (EESS) lies adjacent to the large, monzodioritic Ertsberg Intrusion
 387 that was emplaced over a period of up to 300,000 years (Cloos and Sapiie, 2013; Leys et al.,
 388 2012; Macdonald and Arnold, 1994; Meinert et al., 1997; Mertig et al., 1994;
 389 Paterson and Cloos, 2005; Pollard and Taylor, 2002). No specific evidence is preserved of
 390 any eruptive activity relating to its near-surface (<0.5 km) emplacement. Nevertheless, the extensive
 391 EESS alteration and mineralisation that extends to the present surface implies that the mineralised
 392 skarn system underlay a large area of solfataric alteration at the paleo-surface, as is commonly
 393 observed in quiescently degassing magmatic systems today. Such massive fluid flow requires the
 394 maintenance of a permeable array of faults and fractures such as observed throughout the EESS
 395 (Leys et al., 2012).

396 5.2.2 Pressure-temperature and phase relations of the fluid

397 The fluid of Stage 2 had a temperature of ≥ 600 °C based on fluid inclusion homogenisation
 398 temperatures (Baline, 2007) which is consistent with the upper temperature limit of 750 ± 50 °C for
 399 contact metamorphism assumed in this paper. At the samples' estimated paleo-depths (2.1 ± 0.2 km),
 400 an assumption of a mean density of the overlying sediments provides an upper limit on lithostatic
 401 pressure of 51 ± 5 MPa (see section 5.1.1 *Constraints on the pressure during contact*
 402 *metamorphism*). The highest fluid pressure possible is constrained by the sum of lithostatic
 403 pressure and the tensile strength of the rock (Cox, 2010). The tensile strength of rock ranges
 404 from 0.5-5 MPa so that the highest fluid pressure at the sample depth was therefore a maximum of
 405 56 ± 5 MPa. However, a much lower fluid pressure necessarily occurred in the magmatic fluid phase
 406 as it expanded from its source to the surface (~ 0.1 MPa) through a fault and fracture array, since

$$407 (\rho_{\text{fluid}} * g * h) < (\rho_{\text{rock}} * g * h) \quad (1)$$

408 where ρ is the density, g is acceleration due to gravity and h is the depth. Magmatic fluid expansion in
 409 porphyry copper systems was defined by Weis (2015) and Henley and McNabb (1978) showing the
 410 formation of a low density magmatic vapour plume displacing groundwater. In order to prevent
 411 groundwater swamping the system, the pressure of the magmatic fluid must be above the cold water
 412 hydrostatic pressure at the sample depth. This defines a minimum pressure estimate of 21.5 ± 2 MPa
 413 based on the density of groundwater. Thus, the pressure of the magmatic fluid during alteration and
 414 mineralisation (Stage 2) was therefore between 21.5 ± 2 MPa and 56 ± 5 MPa.

415 It has long been established that the continuum fluid in the formation of porphyry copper and related
 416 deposits is a low salinity gas phase (Henley and McNabb, 1978; Weis et al., 2012); note that the
 417 term 'vapour' applies to a gas phase in equilibrium with a contiguous solid or liquid phase.
 418 Expansion of this phase to lower pressures en route from source to surface results in the formation

419 of a very small (< 2 volume percent) saline liquid phase that is over-represented in fluid inclusion
420 assemblages because of its wetting properties (Mernagh et al., 2020), or halite (Lecumberri-
421 Sanchez et al., 2015; Weis et al., 2012). These phase relationships are shown in Figure 9
422 with reference to the melting regime of diorite and the pressure conditions calculated here for
423 contact metamorphism (Stage 1) and the expansion of a magmatic vapour (Stage 2). Since rock
424 materials are insulators, the expansion path of a magmatic vapour through fracture arrays to the
425 surface is constrained to be irreversible and isenthalpic but may be reversible and isentropic as
426 it is released from the magma into the array (Anderson and Crerar, 1993; Barton and Toulmin,
427 1961). The isenthalpic paths indicated in Figure 9 are for the PT conditions estimated here for our
428 samples from the EESS and show a single phase low density gas phase expanding from a magma
429 complex beneath the system to low pressure towards the surface where they may intersect the liquid
430 + vapour or halite + vapour regions. The phase state projections are shown in enthalpy-pressure
431 space to demonstrate expansion paths for the EESS within the constraints of energy and mass
432 conservation (Mernagh et al., 2020). The use of temperature was omitted, because it is not an
433 extensive property of a fluid phase. For the adjacent Big Gossan Skarn (Fig. 1), Meinert et al. (1997)
434 report silicate compositions and two populations of fluid inclusion in samples taken between 2,900
435 and 3,000 m a.s.l. and therefore closer to the paleosurface than the samples reported here from the
436 EESS. The two populations of fluid inclusions reported by Meinert et al. (1997) are: (1) fluid
437 inclusions with multiple solids like halite, sylvite, chalcocopyrite, hematite and anhydrite in pyroxene
438 crystals with homogenisation temperatures between 360 to 535 °C, a mean salinity of 57 wt%
439 NaCl+KCl_{equiv} and no evidence of phase unmixing ('boiling') for these inclusions; (2) fluid
440 inclusions in quartz and anhydrite which are dominantly vapour-rich but also liquid-rich with an
441 average homogenisation temperature of 369 °C and a salinity of 6-8 wt% NaCl_{equiv}. Based on these
442 two population of fluid inclusions, Meinert et al. (1997) interpreted metamorphism and skarn
443 formation to be contiguous whereas our data, and that from calc-silicate mineralised skarns in the
444 EESS Henley et al. (2017), define the separate stages of contact metamorphism and mineralisation.
445 This is supported by the (partial) replacement of prograde Mg-silicates (e.g. olivine, diopside) by
446 anhydrite (Fig. 6). Furthermore, the widespread alteration of diopside grains evidence metasomatism
447 after diopside formation. Such subsequent, metasomatic overprint was also reported for garnets in
448 calc-silicate skarns Henley et al. (2017). The fluid inclusion data of Meinert et al. (1997) is more
449 rigorously interpreted on the basis of a low salinity, low density, high enthalpy continuum fluid
450 from which a very small amount of high salinity liquid or halite exsolved as described by Mernagh
451 et al. (2020) for the adjacent Grasberg and other copper deposits. The co-existing liquid and
452 vapour inclusions indicate trapping during phase unmixing and subsequent heat transfer from
453 wallrock to produce hypersaline inclusions as described by Mernagh et al. (2020). This approach
454 obviates the otherwise unanswered question of the source of thermal energy (> 2 kJ/kg) to sustain

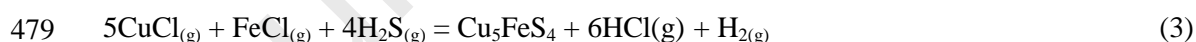
455 boiling in the model proposed by Meinert et al. (1997).

456 5.2.3 Formation of anhydrite and precipitation of Cu

457 The principal Stage 2 alteration observed in sample CS1 and FM1 is the metasomatic replacement of
458 calcite (CaCO_3) by anhydrite (CaSO_4) which may be expressed as the mass balance equation (2).



460 Log (K) for this reaction varies from 8 at 700 °C to 12.3 at 500 °C (K is the equilibrium constant). The
461 reduced sulfur forms Cu-Fe-sulphide minerals from Cu and Fe transported in the general flux of
462 magmatic gas (Henley et al., 2015; Henley and Seward, 2018), the iron largely released from
463 wallrock. This alteration sequence is preserved, for instance, in the NE quadrant of Fig. 4b
464 within the transition into the Mg-rich, forsterite and diopside containing contact zone.
465 Saadatfar et al. (2020) have shown experimentally that this process is kinetically favourable
466 and is sustained by the highly connected porosity of the intergranular anhydrite that develops
467 along grain boundaries in carbonate rock material (see their Fig. 1c-d). Their experiments also
468 showed that percolation channels were maintained through the bulk rock by the anisotropic expansion
469 of calcite and the connectivity of the porous anhydrite product layer along these grain boundaries. In
470 the stressed environment of an active volcanic system tensile fractures are likely to continuously
471 reopen. Because fractures therefore remain permeable, the conversion rate of carbonate to anhydrite
472 through nucleation and growth of anhydrite crystals is only limited by the rates of ingress and
473 egress of reactant and product gases at the reaction front of each calcite grain. The deposition of
474 economic amounts of Cu-Fe-sulphides within the altered and metasomatised regions of CS1 and, with
475 anhydrite in FM1, provides evidence of the pervasive flow of metal-bearing, magma-derived fluid in
476 Stage 2. It is the *in situ* generation of $\text{H}_2\text{S}(g)$ that drives economic copper deposition (as bornite)
477 due to its very low solubility as is observed in sample FM1 and throughout the system. Bornite
478 deposition may be represented by the synoptic mass-balance reaction equation,



480 for which log (K) at 700 °C is 4×10^{54} and 3.8×10^{63} at 600 °C. The reaction is written using the
481 dominant Cu and Fe species determined elsewhere for magmatic arc volcanic gases (Henley and
482 Seward, 2018). The speciation of metals in high temperature gas mixtures is complex so that other Fe
483 and Cu species occur at lower concentrations and in an equilibrium model any one of them may be
484 used to express solubility reactions but the speciation shown here expresses the highest contribution
485 to bornite solubility noting that at much higher initial sulfur concentrations the species $\text{Cu}_2\text{S}(g)$ may
486 become important. Although the EESS is of economic importance of its copper content, the
487 sulphur anomaly that the deposit represents is compelling in terms of the volume of rock that
488 experiences the addition of sulphur. Extensive drilling data (kindly provided by P.T. Freeport
489 Indonesia) show that the amount of forsterite-dominated skarn in the EESS is ~1,485 Mt.

490 Considering the abundance of anhydrite observed in the sample FM1, the amount of anhydrite
491 within the forsterite-dominated skarns of the EESS is ~1,100 Mt (Table S2 in the supplementary
492 information). The implication of reaction (2) is that metasomatism of the carbonate sediment
493 formed this amount of anhydrite and required a total flux of ~1,050 Mt of $\text{SO}_2(\text{g})$. Hughes et
494 al. (2016) reported $\text{SO}_2(\text{g})$ flux data for arc volcanic gases from modern volcanoes as between
495 ~73 to 21,000 tonnes per day with a median $\text{SO}_2(\text{g})$ flux of 735 tonnes per day. Using this median
496 $\text{SO}_2(\text{g})$ flux, the lifetime of the degassing EESS system could have been around 3,900 years (Table
497 S2 in the supplementary information). In order to sustain such flux during Stage 2 at the relatively
498 shallow paleo-depth of the system, the fracture array would necessarily have been open to the
499 surface and sustained a range of shallow hydrothermal phenomena such as fumaroles and solfatara.

500 5.3 Stage 3: Retrograde hydration

501 Retrograde alteration (Stage 3) occurred when the magmatic system waned resulting in a decrease in
502 temperature and magmatic vapour flux compared to the skarn mineralisation stage (Stage 2). H_2O -
503 rich fluids trapped during Stage 2 or flooding from the surrounding country rock into the mineralised
504 skarns (e.g., Fig. 15 in King et al. (2018)) caused retrograde hydration. The lack of retrograde
505 carbonation indicates relatively low $X_{\text{CO}_2(\text{g})}$ in the ambient fluid (forsterite and diopside are not
506 carbonated, but partially hydrated to serpentine (Fig. 3 and 5a)). Anhydrite is preserved because the
507 temperatures were relatively high at the low pressures of serpentinization (e.g. Blounot and Dickson
508 (1969); Fig. 16 in King et al. (2018)).

509 6 Conclusions

510 We have here described the development of mineralised Mg-silicate skarns in the East Ertsberg Skarn
511 System from contact metamorphism of carbonate-rich sediments by the Ertsberg Intrusion (Stage 1 at
512 2.7-2.9 Ma), through subsequent high temperature alteration by a flux of magmatic gas (Stage 2) to
513 subsequent overprinting by retrograde, hydrothermal alteration (Stage 3). During contact
514 metamorphism (Stage 1), temperatures have here been shown through mineral chemistry and
515 thermochemical analysis to have reached 750 ± 50 °C at the sample depth where lithostatic pressure
516 was 51 ± 5 MPa. In Stage 2, the flux of magmatic gas from the Ertsberg Intrusion resulted in the
517 conversion of members of the New Guinea Limestone Group to mineralised skarns and replacement
518 bodies up to 1 km from the igneous contact and a paleodepth range from about 0.5 to over 2.5 km
519 (Fig. 1d). Typical porphyry copper alteration and mineralisation occurs in the Ertsberg intrusion but
520 magmatic gas expansion was mainly channeled through the embrittled, contact-metamorphosed
521 marble sequence. The combination of continuing tectonic and thermal stress with the generation of
522 porous anhydrite maintained the high permeability of this sequence and sustains bulk sulphate
523 metasomatism and Cu mineralisation within >2,600 Mt of exoskarns. About 60 wt% of this exoskarn

524 was converted from a carbonate-rich assemblage to one dominated by forsterite, anhydrite and
525 sulphide minerals. Geologic data show that these processes operated to within one kilometer of the
526 paleo-surface and required the throughput of at least 1,050 Mt of $\text{SO}_2(\text{g})$. The hydrodynamic and
527 chemical environment responsible for mineralisation within the EESS is similar to those responsible
528 for the formation of sub-volcanic porphyry copper systems (Henley and McNabb, 1978;
529 Jochum et al., 2012; Lecumberri-Sanchez et al., 2015) where a magmatic fluid phase
530 expands through the upper crust to form a gas-dominated hydrodynamic plume that vents to the
531 surface. Most porphyry copper systems are hosted by intrusive and related volcanic rocks but in the
532 EESS much of the flux was focussed through and mineralised the contact metamorphosed and
533 embrittled carbonate sequence, while dispersion through the upper part of the Ertsberg intrusion
534 formed porphyry copper and endoskarn-style alteration and mineralisation. The context for skarn
535 alteration and mineralisation provided here is therefore compatible with the occurrence of low grade
536 *porphyry copper* style alteration and mineralisation in the upper part of the Ertsberg intrusion (Leys
537 et al., 2012). In other words it is a consequence of reactive mass transport in a magmatic vapour
538 plume (Henley and McNabb, 1978; Henley et al., 2015; Weis, 2015; Weis et al.,
539 2012) fluxing from an intrusive source regime through fractured reactive (meta-) sedimentary rock
540 to surface.

541 **7 Acknowledgments**

542 This study was partially supported by Australian Research Council funding to P. King (DP150104604
543 and FT130101524). We thank staff at the Centre for Advance Microscopy (CAM), ANU for their help
544 and acknowledge its funding as part of NCRIS Microscopy Australia. And we thank Terry
545 Mernagh for critical comment of previously published fluid inclusion data from Ertsberg. We
546 thank PT. Freeport for samples and drill core data. Further, we thank two anonymous reviewer for
547 constructive comments and F. Pirajno for the editorial handling of this paper.

548 **8 References**

- 549 Anderson, G. M., and Crerar, D. A., 1993, Thermodynamics in geochemistry: The equilibrium model,
550 Oxford University Press on Demand.
- 551 Baline, L. M., 2007, Hydrothermal Fluids and Cu-Au Mineralization of the Deep Grasberg Porphyry
552 Deposit, Papua, Indonesia [Thesis: University of Texas, Austin, 287 p.
- 553 Barton, P. B., and Toulmin, P., 1961, Some mechanisms for cooling hydrothermal fluids: US
554 Geological Survey Professional Paper, v. 424, p. 348-352.
- 555 Blounot, C., and Dickson, F., 1969, The solubility of anhydrite (CaSO_4) in $\text{NaCl-H}_2\text{O}$ from 100 to
556 450 C and 1 to 1000 bars: *Geochimica et Cosmochimica Acta*, v. 33, no. 2, p. 227-245.
- 557 Bucher-Nurminen, K., 1982, Mechanism of Mineral Reactions Inferred from Textures of Impure
558 Dolomitic Marbles from East Greenland: *Journal of Petrology*, v. 23, no. 3, p. 325-343.
- 559 Bucher, K., and Grapes, R., 2011, Metamorphism of Dolomites and Limestones, *Petrogenesis of*
560 *Metamorphic Rocks*, Springer, p. 225-255.
- 561 Cloos, M., and Sapiie, B., 2013, Porphyry copper deposits: strike-slip faulting and throttling cupolas:
562 *International Geology Review*, v. 55, no. 1, p. 43-65.
- 563 Connolly, J. A. D., 2009, The geodynamic equation of state: What and how: *Geochemistry*

- 564 Geophysics Geosystems, v. 10, no. 10, p. 1525-2027.
- 565 Cox, S. F., 2010, The application of failure mode diagrams for exploring the roles of fluid pressure
566 and stress states in controlling styles of fracture-controlled permeability enhancement in
567 faults and shear zones: *Geofluids*, v. 10, no. 1-2, p. 217-233.
- 568 Diener, J. F. A., and Powell, R., 2012, Revised activity-composition models for clinopyroxene and
569 amphibole: *Journal of Metamorphic Geology*, v. 30, no. 2, p. 131-142.
- 570 Driesner, T., 2007, The system H₂O–NaCl. Part II: Correlations for molar volume, enthalpy, and
571 isobaric heat capacity from 0 to 1000° C, 0 to 5000bar, and 0 to 1 X NaCl: *Geochimica et*
572 *Cosmochimica Acta*, v. 71, no. 20, p. 4902-4919.
- 573 Einaudi, M. T., and Burt, D. M., 1982, A Special Issue Devoted to Skarn Deposits - Introduction -
574 Terminology, Classification, and Composition of Skarn Deposits: *Economic Geology*, v. 77,
575 no. 4, p. 745-754.
- 576 Fuhrman, M., and Lindsley, D., 1988, Feldspar minerals: *American Mineralogist*, v. 73, p. 201-215.
- 577 Fulignati, P., Kamenetsky, V. S., Marianelli, P., Sbrana, A., and Mernagh, T. P., 2001, Melt inclusion
578 record of immiscibility between silicate, hydrosaline, and carbonate melts: Applications to
579 skarn genesis at Mount Vesuvius: *Geology*, v. 29, no. 11, p. 1043-1046.
- 580 Gandler, L., 2006, Calc-silicate alteration and Cu-Au mineralization of the Deep MLZ skarn; Ertsberg
581 District, Papua, Indonesia [Master Thesis Master]: University of Texas, Austin.
- 582 Gibbins, S. L., 2006, The Magmatic and Hydrothermal Evolution of the Ertsberg Intrusion in the
583 Gunung Bijih (Ertsberg) Mining District, West Papua, Indonesia [PhD Thesis PhD]:
584 University of Arizona, 384 p.
- 585 Harrison, J. S., 1999, Hydrothermal alteration and fluid evolution of the Grasberg porphyry Cu-Au
586 deposit, Irian Jaya, Indonesia [Master Thesis Master]: University of Texas, Austin, 205 p.
- 587 Henley, R., and McNabb, A., 1978, Magmatic vapor plumes and ground-water interaction in porphyry
588 copper emplacement: *Economic Geology*, v. 73, no. 1, p. 1-20.
- 589 Henley, R. W., Brink, F. J., King, P. L., Leys, C., Ganguly, J., Mernagh, T., Middleton, J., Renggli, C.
590 J., Sieber, M., Troitzsch, U., and Turner, M., 2017, High temperature gas-solid reactions in
591 calc-silicate Cu-Au skarn formation; Ertsberg, Papua Province, Indonesia: *Contributions to*
592 *Mineralogy and Petrology*, v. 172, no. 11-12, p. 106.
- 593 Henley, R. W., and Hughes, G. O., 2016, SO₂ flux and the thermal power of volcanic eruptions:
594 *Journal of Volcanology and Geothermal Research*, v. 324, p. 190-199.
- 595 Henley, R. W., King, P. L., Wykes, J. L., Renggli, C. J., Brink, F. J., Clark, D. A., and Troitzsch, U.,
596 2015, Porphyry copper deposit formation by sub-volcanic sulphur dioxide flux and
597 chemisorption: *Nature Geoscience*, v. 8, no. 3, p. 210-215.
- 598 Henley, R. W., and Seward, T. M., 2018, Gas-Solid Reactions in Arc Volcanoes: Ancient and
599 Modern: *High Temperature Gas-Solid Reactions in Earth and Planetary Processes*, v. 84, no.
600 1, p. 309-349.
- 601 Holland, T., and Powell, R., 1991, A compensated-Redlich-Kwong (CORK) equation for volumes
602 and fugacities of CO₂ and H₂O in the range 1 bar to 50 kbar and 100–1600C: *Contributions*
603 *to Mineralogy and Petrology*, v. 109, no. 2, p. 265-273.
- 604 -, 2003, Activity–composition relations for phases in petrological calculations: an asymmetric
605 multicomponent formulation: *Contributions to Mineralogy and Petrology*, v. 145, no. 4, p.
606 492-501.
- 607 Holland, T. J. B., and Powell, R., 1998, An internally consistent thermodynamic data set for phases of
608 petrological interest: *Journal of Metamorphic Geology*, v. 16, no. 3, p. 309-343.
- 609 -, 2011, An improved and extended internally consistent thermodynamic dataset for phases of
610 petrological interest, involving a new equation of state for solids: *Journal of Metamorphic*
611 *Geology*, v. 29, no. 3, p. 333-383.
- 612 Holtz, F., Becker, A., Freise, M., and Johannes, W., 2001, The water-undersaturated and dry Qz-Ab-
613 Or system revisited. Experimental results at very low water activities and geological
614 implications: *Contributions to Mineralogy and Petrology*, v. 141, no. 3, p. 347-357.
- 615 Hughes, J. M., Harlov, D., Kelly, S. R., Rakovan, J., and Wilke, M., 2016, Solid solution in the apatite
616 OH-Cl binary system: Compositional dependence of solid-solution mechanisms in calcium
617 phosphate apatites along the Cl-OH binary: *American Mineralogist*, v. 101, no. 8, p. 1783-
618 1791.

- 619 Jochum, K. P., Scholz, D., Stoll, B., Weis, U., Wilson, S. A., Yang, Q., Schwalb, A., Börner, N.,
620 Jacob, D. E., and Andreae, M. O., 2012, Accurate trace element analysis of speleothems and
621 biogenic calcium carbonates by LA-ICP-MS: *Chemical Geology*, v. 318, p. 31-44.
- 622 King, P. L., Wheeler, V. M., Renggli, C. J., Palm, A. B., Wilson, S. A., Harrison, A. L., Morgan, B.,
623 Nekvasil, H., Troitzsch, U., Mernagh, T., Yue, L., Bayon, A., DiFrancesco, N. J., Baile, R.,
624 Kreider, P., and Lipinski, W., 2018, Gas-Solid Reactions: Theory, Experiments and Case
625 Studies Relevant to Earth and Planetary Processes: *High Temperature Gas-Solid Reactions in*
626 *Earth and Planetary Processes*, v. 84, no. 1, p. 1-56.
- 627 Kullerud, G., Yund, A., and Moh, G., 1969, Phase relation in the Cu-Fe-S, Cu-Ni-S and Fe-Ni-S
628 System: *Carnegie Institute of Washington Year Book*, v. 15, p. 323-343.
- 629 Kyle, J. R., Gandler, L., Mertig, H., Rubin, J., and Ledvina, M., 2014, Stratigraphic Inheritance
630 Controls of Skarn-hosted Metal Concentrations: Ore controls for Ertsberg-Grasberg District
631 Cu-Au skarns, Papua, Indonesia: *Acta Geologica Sinica (English Edition)*, v. 88, no. s2, p.
632 529-531.
- 633 Lecumberri-Sanchez, P., Steele-MacInnis, M., Weis, P., Driesner, T., and Bodnar, R. J., 2015, Salt
634 precipitation in magmatic-hydrothermal systems associated with upper crustal plutons:
635 *Geology*, v. 43, no. 12, p. 1063-1066.
- 636 Leys, C. A., Cloos, M., New, B. T., and MacDonald, G. D., 2012, Copper-gold±molybdenum deposits
637 of the Ertsberg-Grasberg District Papua, Indonesia: *Society of Economic Geologists, Special*
638 *Publication*, v. 16, p. 215-235.
- 639 Macdonald, G. D., and Arnold, L. C., 1994, Geological and Geochemical Zoning of the Grasberg
640 Igneous Complex, Irian-Jaya, Indonesia: *Journal of Geochemical Exploration*, v. 50, no. 1-3,
641 p. 143-178.
- 642 Matthews, S. J., Marquillas, R. A., Kemp, A. J., Grange, F. K., and Gardeweg, M. C., 1996, Active
643 skarn formation beneath Lascar Volcano, northern Chile: a petrographic and geochemical
644 study of xenoliths in eruption products: *Journal of Metamorphic Geology*, v. 14, no. 4, p. 509-
645 530.
- 646 McMahon, T. P., 1994, Pliocene Intrusions in the Gunung Bijih (Ertsberg) Mining District, Irian Jaya,
647 Indonesia: *Petrography and Mineral Chemistry: International Geology Review*, v. 36, no. 9, p.
648 820-849.
- 649 Meinert, L. D., Dipple, G. M., and Nicolescu, S., 2005, World skarn deposits: *Economic Geology* v.
650 *100th Anniversary Volume*, p. 299-336.
- 651 Meinert, L. D., Hefton, K. K., Mayes, D., and Tasiran, I., 1997, Geology, zonation, and fluid
652 evolution of the big Gossan Cu-Au skarn deposit, Ertsberg district: Irian Jaya: *Economic*
653 *Geology and the Bulletin of the Society of Economic Geologists*, v. 92, no. 5, p. 509-534.
- 654 Mernagh, T., Leys, C., and Henley, R. W., 2020, Fluid inclusion systematics in porphyry copper
655 deposits: The super-giant Grasberg deposit, Indonesia, as a case study: *Ore Geology Reviews*,
656 v. 123.
- 657 Mertig, H. J., 1995, *Geology and Ore Formation of the Dom Copper Skarn Deposit, Ertsberg*
658 *(Gunung Bijih) District, Irian Jaya, Indonesia* [Master]: University of Texas.
- 659 Mertig, H. J., Rubin, J. N., and Kyle, J. R., 1994, Skarn Cu-Au Orebodies of the Gunung-Bijih
660 (Ertsberg) District, Irian-Jaya, Indonesia: *Journal of Geochemical Exploration*, v. 50, no. 1-3,
661 p. 179-202.
- 662 Paterson, J. T., and Cloos, M., 2005, Grasberg porphyry Cu–Au deposit, Papua, Indonesia: 1.
663 Magmatic history, South Australia, PGC Publishing, Super porphyry copper and gold
664 deposits: A global perspective, 313-330 p.:
- 665 Pirajno, F., 2013, *Effects of Metasomatism on Mineral Systems and Their Host Rocks: Alkali*
666 *Metasomatism, Skarns, Greisens, Tourmalinites, Rodingites, Black-Wall Alteration and*
667 *Listvenites, Metasomatism and the Chemical Transformation of Rock: The Role of Fluids in*
668 *Terrestrial and Extraterrestrial Processes*: Berlin, Heidelberg, Springer Berlin Heidelberg, p.
669 203-251.
- 670 -, 2018, Halogens in hydrothermal fluids and their role in the formation and evolution of
671 hydrothermal mineral systems, *The Role of Halogens in Terrestrial and Extraterrestrial*
672 *Geochemical Processes*, Springer, p. 759-804.
- 673 Pollard, P. J., and Taylor, R. G., 2002, Paragenesis of the Grasberg Cu-Au deposit, Irian Jaya,

- 674 Indonesia: results from logging section 13: *Mineralium Deposita*, v. 37, no. 1, p. 117-136.
- 675 Proyer, A., Mposkos, E., Bazicitis, I., and Hoinkes, G., 2008, Tracing high-pressure metamorphism in
676 marbles: Phase relations in high-grade aluminous calcite-dolomite marbles from the Greek
677 Rhodope massif in the system CaO-MgO-Al₂O₃-SiO₂-CO₂ and indications of prior
678 aragonite: *Lithos*, v. 104, no. 1-4, p. 119-130.
- 679 Saadatfar, M., Brink, F., Latham, S., King, P., Middleton, J., Troitzsch, U., Turner, M., and Henley,
680 R. W., 2020, High resolution 3D mapping of grain kinematics during high temperature
681 sequestration of SO₂ from flue gas by carbonate aggregates: *Sci Rep*, v. 10, no. 1, p. 2201.
- 682 Satish-Kumar, M., Wada, H., Santosh, M., and Yoshida, M., 2001, Fluid-rock history of granulite
683 facies humite-marbles from Ambasamudram, southern India: *Journal of Metamorphic
684 Geology*, v. 19, no. 4, p. 395-410.
- 685 Skippen, G., 1974, An experimental model for low pressure metamorphism of siliceous dolomitic
686 marble: *American Journal of Science*, v. 274, no. 5, p. 487-509.
- 687 Thu, Y. K., and Enami, M., 2018, Evolution of metamorphic fluid recorded in granulite facies
688 metacarbonate rocks from the middle segment of the Mogok metamorphic belt in central
689 Myanmar: *Journal of Metamorphic Geology*, v. 36, no. 7, p. 905-931.
- 690 Turner, F. J., 1981, *Metamorphic petrology: Mineralogical, field, and tectonic aspects*, Washington,
691 New York, and London (McGraw Hill), McGraw-Hill Companies.
- 692 Wafforn, S., 2017, *Geo-and Thermochronology of the Ertzberg-Grasberg Cu-Au Mining District,*
693 *West New Guinea, IndonesiaPhD]: University of Texas.*
- 694 Wafforn, S., Seman, S., Kyle, J. R., Stockli, D., Leys, C., Sonbait, D., and Cloos, M., 2018, Andradite
695 garnet U-Pb geochronology of the big Gossan skarn, Ertzberg-Grasberg mining district,
696 Indonesia: *Economic Geology*, v. 113, no. 3, p. 769-778.
- 697 Warren, J. K., 2016, *Magma-Evaporite-Hydrothermal Metal Associations, Evaporites: Switzerland,*
698 *Springer, Cham, p. 1591-1657.*
- 699 Weis, P., 2015, The dynamic interplay between saline fluid flow and rock permeability in magmatic-
700 hydrothermal systems: *Geofluids*, v. 15, no. 1-2, p. 350-371.
- 701 Weis, P., Dreisner, T., and Heinrich, C. A., 2012, Porphyry-copper ore shells form at stable pressure-
702 temperature fronts within dynamic fluid plumes: *Science*, v. 338, p. 1613-1616.
- 703 Wheller, C. J., and Powell, R., 2014, A new thermodynamic model for sapphirine: calculated phase
704 equilibria in K₂O-FeO-MgO-Al₂O₃-SiO₂-H₂O-TiO₂-Fe₂O₃: *Journal of Metamorphic
705 Geology*, v. 32, no. 3, p. 287-299.
- 706 White, R. W., Powell, R., and Clarke, G. L., 2002, The interpretation of reaction textures in Fe-rich
707 metapelitic granulites of the Musgrave Block, central Australia: constraints from mineral
708 equilibria calculations in the system K₂O-FeO-MgO-Al₂O₃-SiO₂-H₂O-TiO₂-Fe₂O₃:
709 *Journal of Metamorphic Geology*, v. 20, no. 1, p. 41-55.
- 710 Yund, R. A., and Kullerud, G., 1966, Thermal stability of assemblages in the Cu—Fe—S system:
711 *Journal of Petrology*, v. 7, no. 3, p. 454-488.
- 712 Zhu, Q. Q., Xie, G. Q., Mao, J. W., Li, W., Li, Y. H., Wang, J., and Zhang, P., 2015, Mineralogical
713 and sulfur isotopic evidence for the incursion of evaporites in the Jinshandian skarn Fe
714 deposit, Edong district, Eastern China: *Journal of Asian Earth Sciences*, v. 113, p. 1253-1267.

715

716 Figure Captions

717 **Fig. 1** (a) Ertzberg district geological map modified after Henley et al. (2017), (b) EESS geological
718 map at a 1.7 km elevation plane, and (c) Cross-section of the Ertzberg East Skarn System provided
719 by PT Freeport Indonesia; (b) and (c) show the drill hole TE06-24 from which the investigated
720 samples (CS1 and FM1) were taken. The samples (CS1 and FM1) come from the Waripi Formation
721 (Tw) which is the lowest formation within the New Guinea Limestone Group. (d) Schematic
722 projection of the relative position and scale of alteration and mineralisation for the EESS, the

723 slightly older Grasberg porphyry copper system (and its open pit mine outline), and other district
724 skarn deposits, modified after Leys et al. (2012). Note that this figure shows the location and extent
725 of mineralisation rather than geological data.

726 **Fig. 2** Si-Ca-Mg+Fe ternary diagram comparing the reconstructed bulk composition of the
727 investigated samples, CS1 (circles) and FM1 (triangle), to the seven stratigraphic units of
728 unmetamorphosed and unaltered sediments of the Waripi Formation (squares) studied by Gandler
729 (2006) and to ICP-AES bulk rock data of exoskarns from the Waripi Formation (data kindly
730 provided from Freeport Indonesia). The plotted exoskarns (diamonds) were collected within a
731 distance of 15 to 150 m to CS1 and FM1. The reconstructed bulk composition of sample FM1
732 correlates reasonably well to limestones and sandy dolostones of the unmetamorphosed Waripi
733 Formation. Like the Waripi-exoskarns, CS1-lower-contact and CS1-Mg-rich-silicate have higher
734 Mg+Fe and lower Si compared to the unaltered sediments.

735 **Fig. 3** Sample FM1: (a, b) TMQEMSCAN maps visualising the phase distribution of anhydrite and
736 forsterite dominated sample FM1. (c) BSE-image of prograde forsterite with phlogopite inclusions
737 and retrograde hydration to serpentine + magnetite at the rim. Abbreviations are: anh: anhydrite;
738 phl: phlogopite; mt2: magnetite likely formed in Stage 2 (associated with anhydrite); mt3:
739 magnetite likely formed in Stage 3 associated with serpentinization of olivine.

740 **Fig. 4** Sample CS1: (a) photography of sample CS1 showing the stratigraphic upper calc-silicate
741 studied by Henley et al. (2017) and the lower Mg-rich silicate investigated in this study. A
742 grossular-diopside assemblage formed during Stage 1 contact metamorphism in the calc-silicate
743 altered into an andradite-anorthite assemblage with anhydrite, chalcopyrite and anorthite selvages
744 during skarn mineralisation (for details see Henley et al. (2017)). The assemblage change through
745 diopside-anhydrite (upper contact) and phlogopite-pargasite (lower contact) into the Mg-silicate
746 containing mainly pargasite, forsterite and diopside. The mineralogy of the contact zone and the
747 Mg-silicate is shown in (b) by the TMQEMSCAN map. In the contact zone and in the Mg-rich
748 silicate, diopside, forsterite, phlogopite, pargasite and Al-spinel (plus calcite) are formed during
749 contact metamorphic. Anhydrite and Fe-Cu-sulphides evidence the input of a magmatic, SO₂-rich
750 gas during Stage (2) alteration. Serpentine (and magnetite) are formed during retrograde hydration
751 (Stage 3). (c) Shows higher resolution detail for part of the altered Mg-silicate-anhydrite-sulphide
752 assemblage in order to define timing relations for mineral phases.

753 **Fig. 5** Sample CS1: (a) detailed TMQEMSCAN map visualising the mineral assemblage and
754 textures discussed in the text for the diopside-anhydrite rich, upper part of the contact zone, for the
755 pargasite-phlogopite rich, lower part of the contact zone and the pargasite-forsterite rich Mg-
756 silicate. The location of the displayed detailed TMQEMSCAN is indicated in the photography of the
757 sample (see Fig. 4). (b, c) Highlighting the textures and phase relations, areas of the (b) pargasite-

758 phlogopite contact zone and (c) from the pargasite-forsterite dominated Mg-silicate.

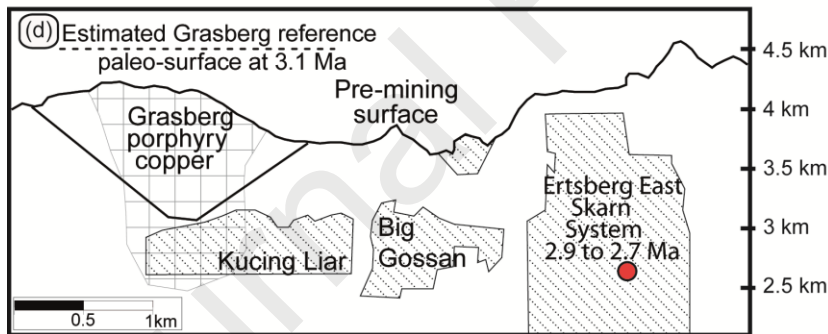
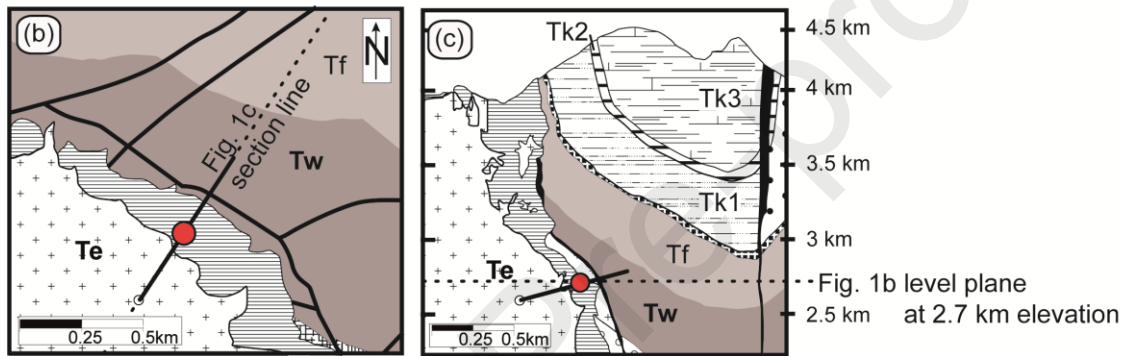
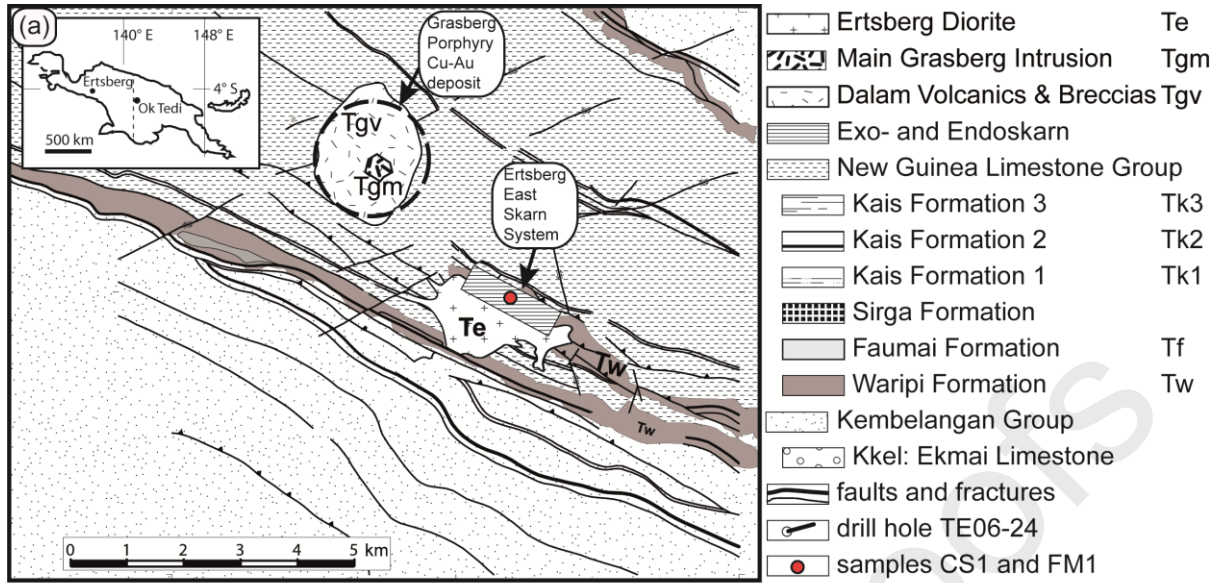
759 **Fig. 6** BSE-image of diopside grain evidencing significant variations in respect to the Mg# of
 760 diopside (numbers refer to Mg# of diopside). The irregular shape of the diopside grain and the
 761 compositional variation within the diopside grain indicate partial alteration of diopside during Stage
 762 2 sulphate metasomatism.

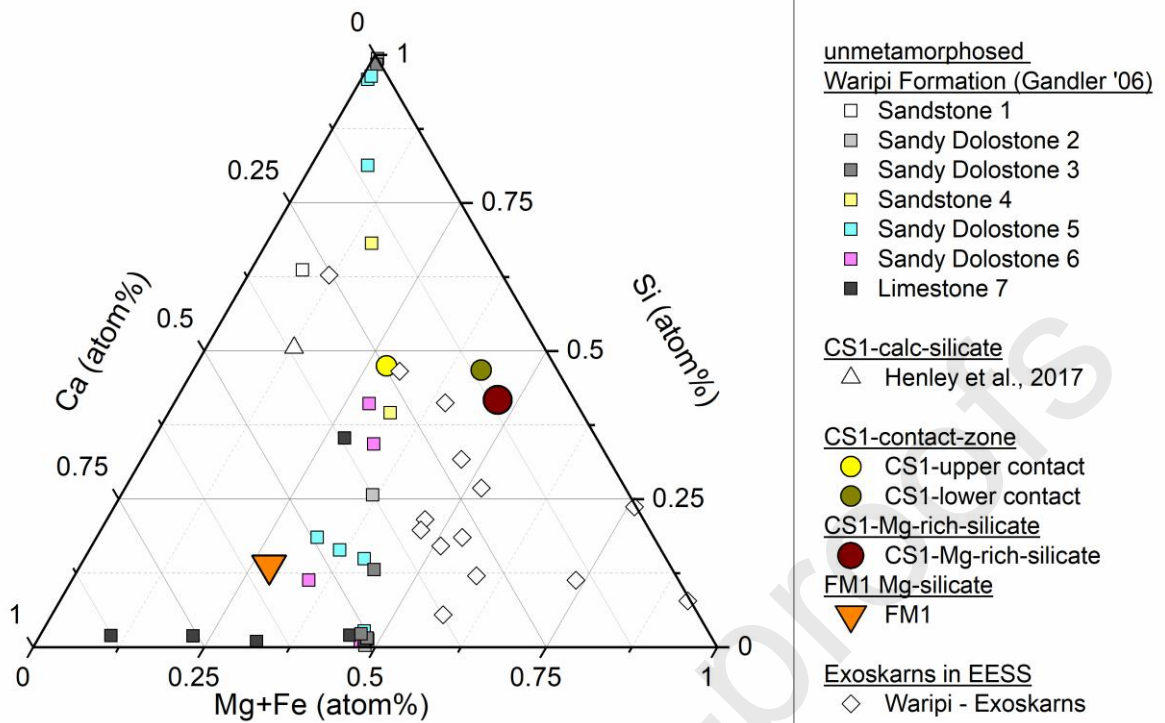
763 **Fig. 7** (a-d) BSE-images of Cu-Fe-sulphides associated with anhydrite from CS1; (e) ternary Cu-
 764 Fe-S diagram at 700 °C after Kullerud et al. (1969); Yund and Kullerud (1966) showing
 765 compositional variability of Cu-Fe-sulphides. Some measurements spots are indicated in the BSE-
 766 images (c-d). Abbreviations and symbols: Anh: anhydrite; Bor: bornite (circle); Cal: Chalcocite
 767 (rectangle); Cp: Chalcopyrite; Fe: iron; Po: pyrrhotite; Phl: phlogopite; S_L: S-bearing liquid

768 **Fig. 8** The main phase relations of the isobaric temperature- $X_{\text{CO}_2}^{\text{fluid}}$ pseudosections modelled at 51
 769 MPa for (a) the Mg-rich part of CS1 and (b) for sample FM1 are shown. The model assumes that
 770 the system is saturated with a CO₂-H₂O fluid. Recalculated bulk rock compositions, used in the
 771 modelling, are reported in Table 1. Temperature- $X_{\text{CO}_2}^{\text{fluid}}$ relations discussed in greater detail in the
 772 text are highlighted. Coloured solid lines refer to mineral-out reactions with increasing temperature.
 773 [1] Cpx Sp cAmph mont ak kls; [2] Cpx Sp cAmph mont ne kls; [3] Cpx Bi cAmph Sp mont kls;
 774 [4] Carb Cpx Sp cAmph kls; [5] Carb Chl Bi Cpx cAmph naph; [6] Carb Chl Bi Cpx cAmph nap;
 775 [7] Chl Bi Carb Cpx nap; [8] Chl Bi Carb Cpx oAmph naph; [9] Chl Bi Carb Cpx naph dol; [10]
 776 Chl Bi Cpx cAmph naph dol; [11] Chl Bi Cpx cAmph dol; [12] Carb Bi Sp Ol mont wu; [13] Carb
 777 Bi Ol Sp vsv; [14] Ol Carb Sp ak kls Abbreviations: ak: akermanite; Bi: Biotite; cAmph: clino
 778 Amphibole; Carb: Carbonate; Chl: Chlorite; Cpx: Clinopyroxene; dol: dolomite; kls: kalsinite;
 779 mont: monticellite; naph: Na-phlogopite; ne: nepheline; Sp: Spinel; wu: wustite; vsv: vesuvianite
 780 (capital letters are used to indicate solid solutions and small letters are used for endmember
 781 compositions).

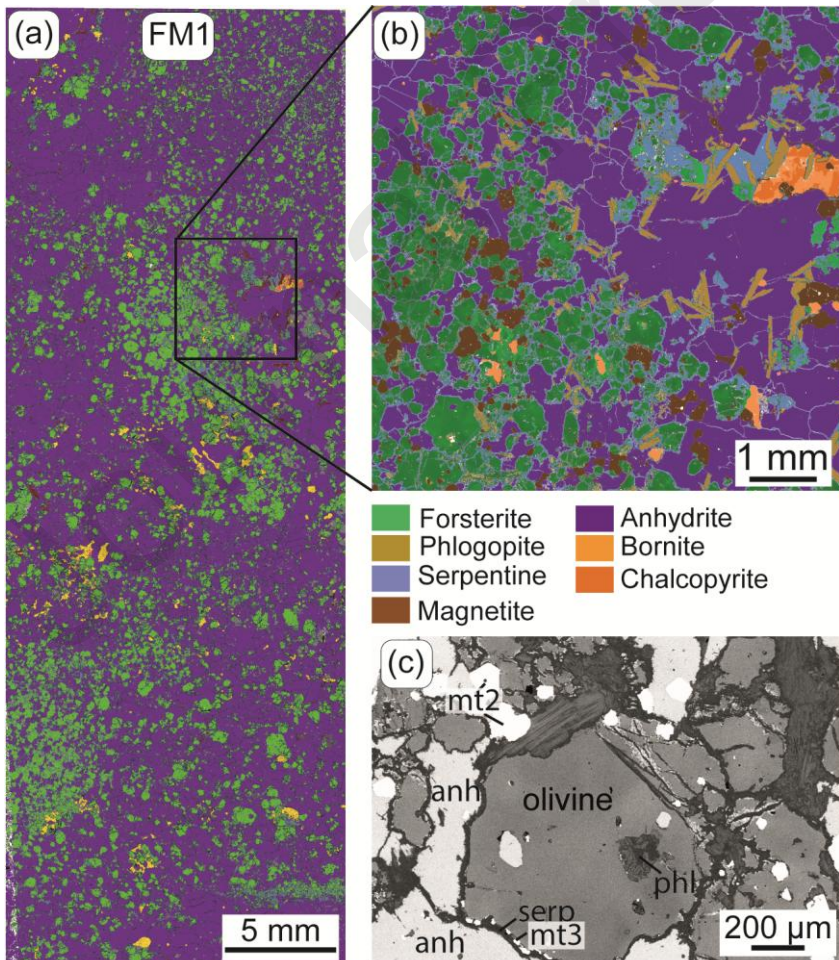
782 **Fig. 9** Isothermic projection of the phase relations and density isopleths for the NaCl-H₂O system
 783 relative to the melting regime of diorite (Holtz et al., 2001). The phase relationships are compiled
 784 from the data of Driesner (2007). The isenthalpic expansion path of a low density, magmatic gas
 785 during Stage 2 (skarn formation and alteration) is shown for the PT conditions estimated here for
 786 our samples from the EESS. Towards the (paleo-) surface the expanding vapour may intersect the
 787 vapour + liquid or vapour + halite regions.

788

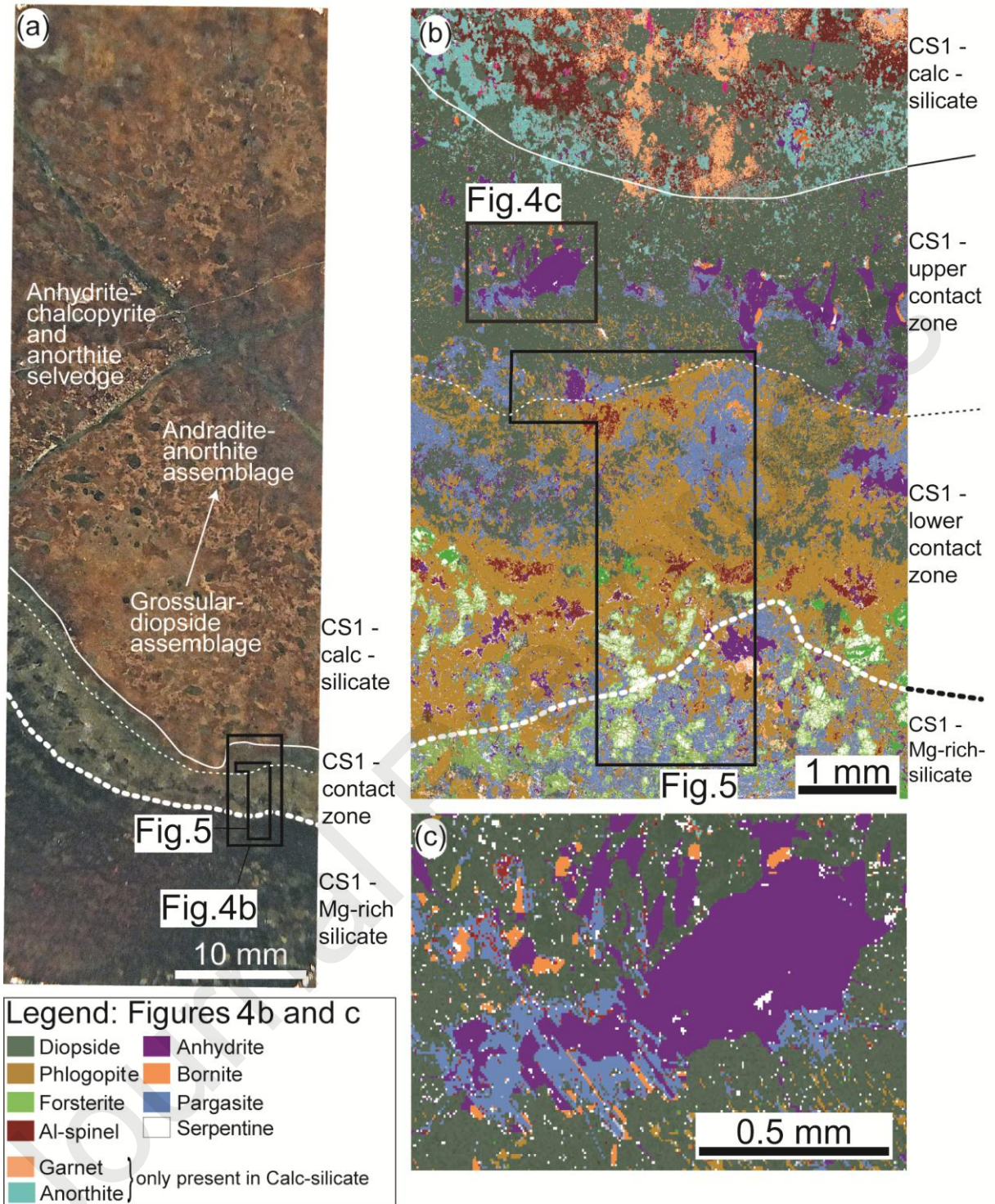




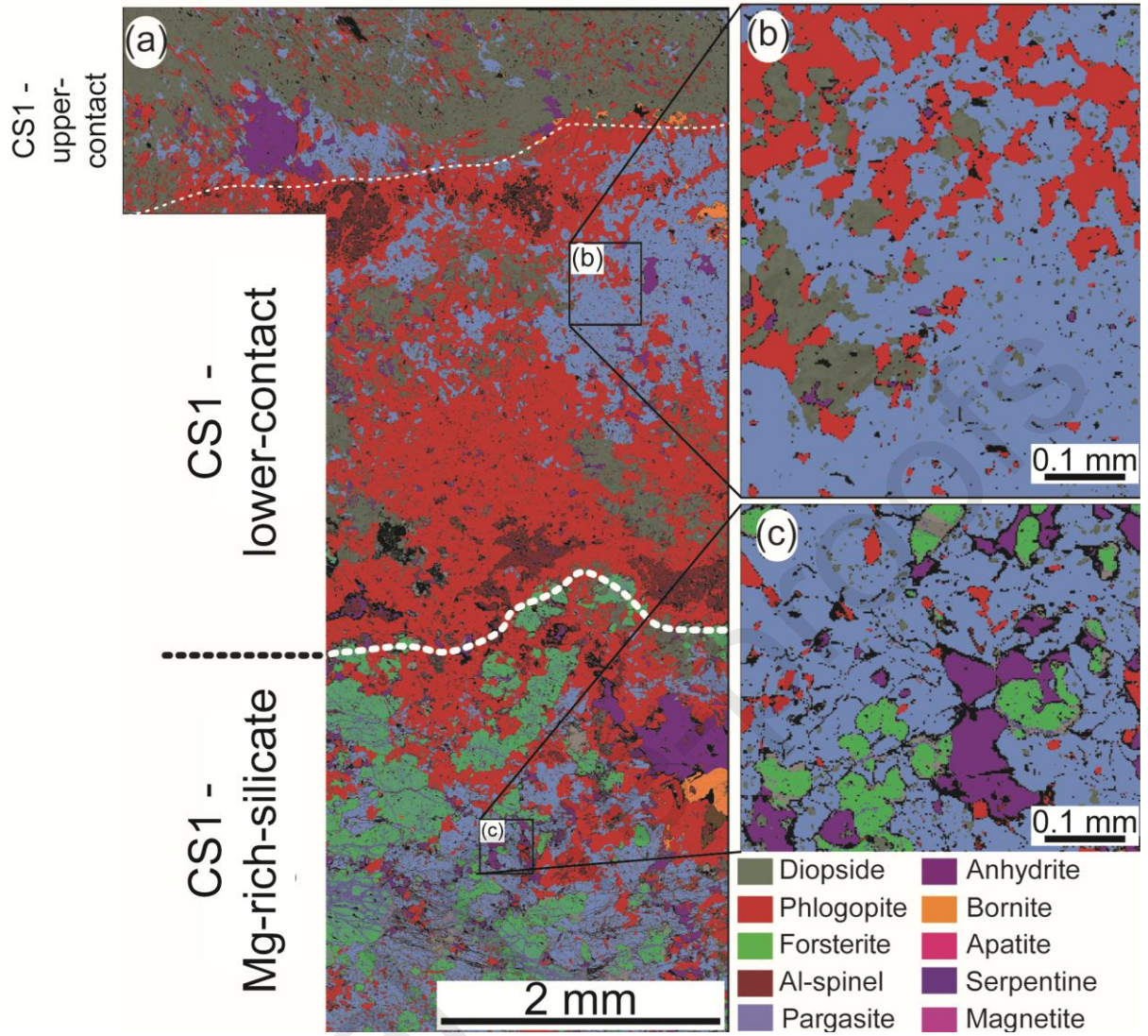
790



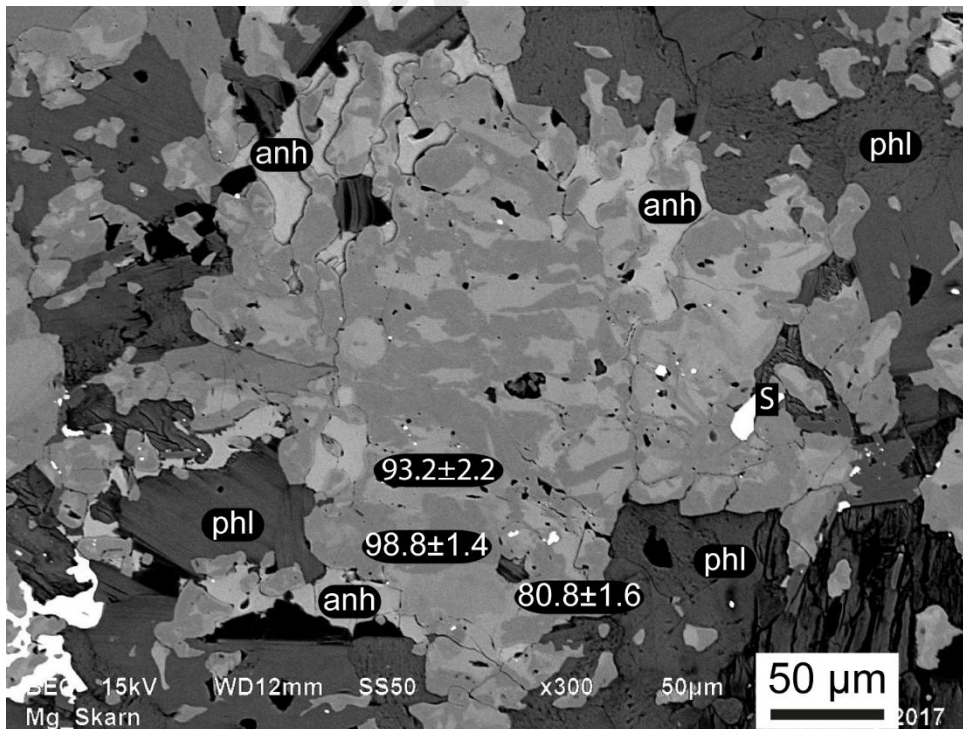
791



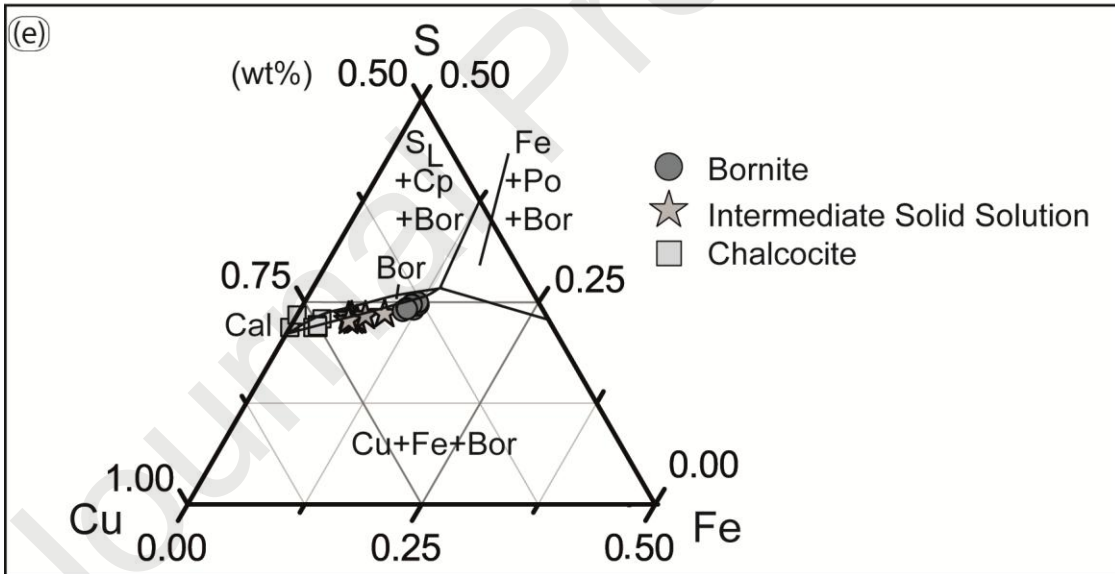
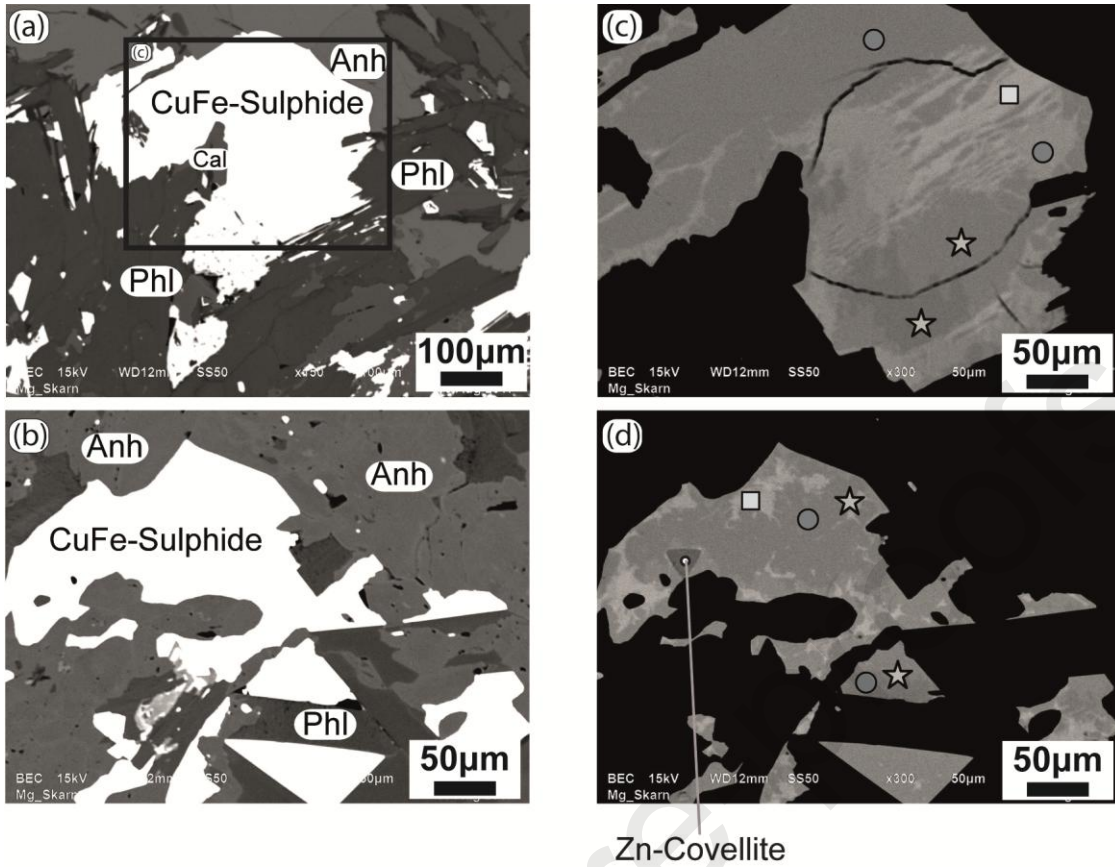
792



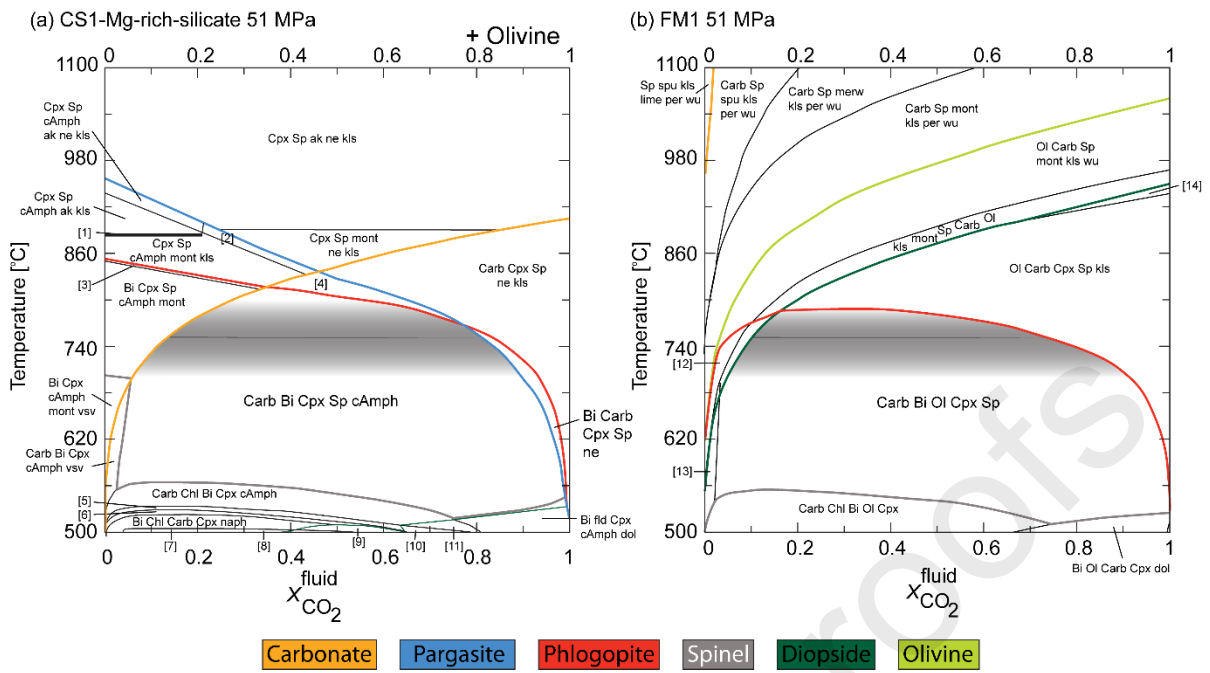
793



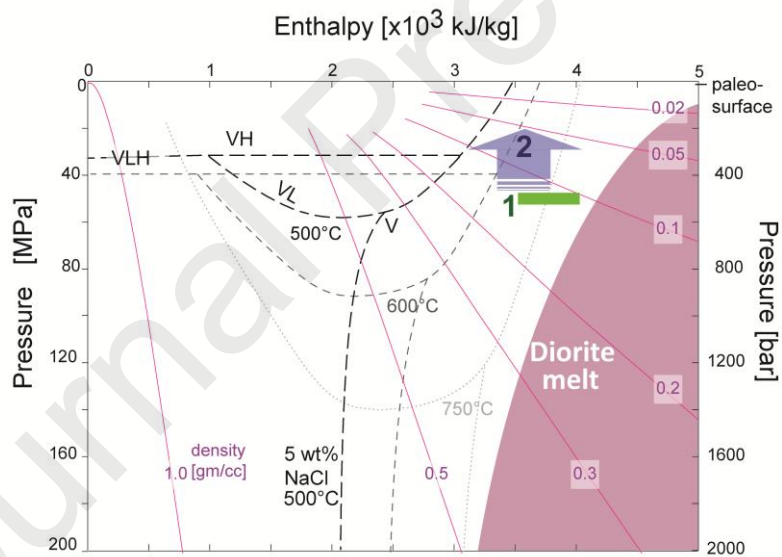
794



795

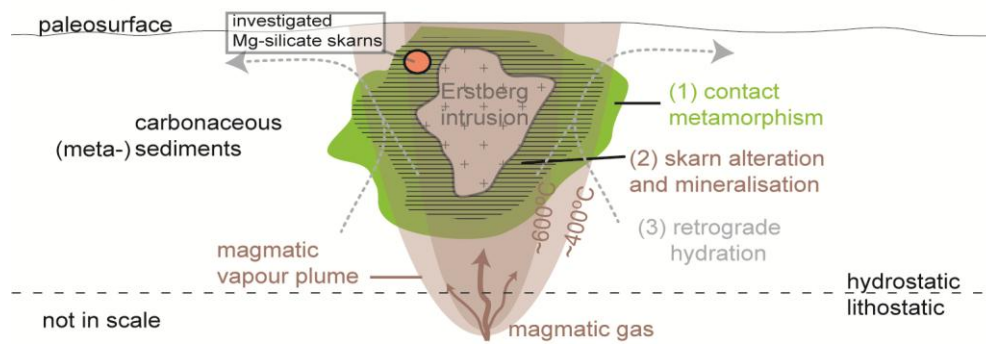


796



797

simplified sketch of fluid-rock interaction detailed in this research



798

799

800

801

802

803

804

805

806

807

808

809

810

811

- Contact metamorphism at 51 ± 5 MPa and 750 ± 50 °C formed forsterite + calcite + phlogopite some diopside and spinel and rare pargasite
- A magmatic vapor plume fluxing from an intrusive source regime through fractured (meta-) sedimentary rock to surface converted carbonates into anhydrite and caused precipitation of Cu-Fe-sulphites (e.g. bornite) and pyrite
- Formation of Mg-rich silicate skarn at East Ertsberg Skarn System required a flux of $\sim 1,050$ Mt SO_2 and may lasted for $\sim 3,900$ years.

Table 1. Phase abundances constrained in TMQEMSCAN maps and major element composition of mineral phases per FE-EPMA of the upper and lower contact of sample CS1, the Mg-silicate part of sample CS1 and sample FM1.

Sample	Lithology	mineral phases	Abundances per QEMSCAN Area%	median composition					
				SiO ₂ wt%	TiO ₂ wt%	Al ₂ O ₃ wt%	FeO wt%	MnO wt%	Mg wt%
CS1	calc-silicate [1]	bulk rock		42.83		17.6	6.77		3
CS1	CS1 - upper contact	Diopside	80.0	48.2	<d.l.	2.7	1.8	<d.l.	16
		Phlogopite	11.7	38.6	0.3	18.9	4.1	<d.l.	22
		Pargasite	6.0	39.5	<d.l.	15.7	6.2	<d.l.	17
		Anhydrite	1.9	0.1	<d.l.	<d.l.	<d.l.	<d.l.	0
		Al-spinel	0.1	0.1	<d.l.	62.3	14.4	<d.l.	19
		Garnet	0.1						nA
		Bornite	0.1						nA
		Cr-spinel	0.01						nA
		Recalulated volatile free bulk rock		48.9		5.7	2.5		17
CS1	CS1 - lower contact	Phlogopite	53.7	37.3	<d.l.	16.8	4.1	<d.l.	23
		Pargasite	22.2	39.5	<d.l.	15.7	6.2	<d.l.	17
		Diopside	16.2	48.2	<d.l.	2.7	1.8	<d.l.	16

	Al-Spinel	3.7	0.1	<d.l.	62.3	14.4	<d.l.	19
	Anhydrite	2.7	0.1	<d.l.	<d.l.	<d.l.	<d.l.	0
	Bornite	0.6						
	Cr-spinel	0.5						nA
	Hematite	0.3						nA
	Magnetite	0.1						nA
	Olivine	0.1						nA
	Serpentine	0.03						nA
	Garnet	0.01						nA
	Recalulated volatile free bulk rock		40.6		16.9	4.9		21
CS1	Pargasite	41.8	40.1	0.3	15.6	6.3	<d.l.	17
	Forsterite	25.3	41.0	<d.l.	<d.l.	4.5	<d.l.	53
	Diopside	13.1	51.0	0.4	2.7	2.2	<d.l.	16
	Serpentine	8.6	41.9	<d.l.	0.2	2.4	<d.l.	39
	Phlogopite	7.6	38.8	0.2	16.6	3.7	<d.l.	24
	Anhydrite	3.0	<d.l.	<d.l.	<d.l.	<d.l.	<d.l.	<d
	Bornite	0.3						
	Hematite	0.3						nA
	Al-spinel	0.04						nA
	Magnetite	n.i.	<d.l.	0.3	<d.l.	92.8	0.6	1
	Chlorite	n.i.	34.2	<d.l.	13.4	2.9	<d.l.	35
	Spadaite	n.i.	43.7	<d.l.	<d.l.	6.1	<d.l.	32
	Recalulated volatile free bulk rock		43.2		8.7	4.9		29
FM1	Anhydrite	75.7	<d.l.	<d.l.	<d.l.	<d.l.	<d.l.	<d
	Serpentine	14.9	41.9	<d.l.	0.2	2.4	<d.l.	39
	Magnetite	4.2	<d.l.	0.3	<d.l.	92.8	0.6	1
	Forsterite	4.2	41.0	<d.l.	<d.l.	4.5	<d.l.	53
	Phlogopite	0.7	38.8	0.2	16.6	3.7	<d.l.	24
	Sulfides	n.i.						nA
		Recalulated volatile free bulk rock		15.32		0.09	8.45	

812 apfu: atoms per formula unit
813 <d.l. below detection limit
814 n.A. not analysed with FE-EPMA
815 n.i. not identified in QEMSCAN map
816 $Mg\# = 100 * Mg[mol] / (Mg[mol] + Fe[mol])$
817 [1] Henley et al. (2017)

818

819

820

821 **Table 2.** Results of thermodynamic models for phase abundances and composition of calcite +
 822 forsterite + diopside + phlogopite + spinel for CS1-Mg-rich-silicate and forsterite + diopside +
 823 calcite + phlogopite + spinel + pargasite for sample FM1. Within the stability fields, a change in
 824 fluid composition (and temperature) has minor effects on mineral modes and compositions. The
 825 abundance and composition of mineral phases are here reported at peak metamorphic conditions
 826 (750 °C and 51 MPa) and 50 mol% CO₂ in the interacting H₂O-CO₂ fluid.

Sample	Mineral phases	Abundances of mineral phases per thermodynamic modelling		Composition per thermodynamic m					
		Vol%	wt%	Number Oxygen	Si apfu	Al apfu	Fe apfu	Mg apfu	Ca apfu
Reconstructed bulk composition of FM1	Calcite	77.87	73.13	1				0.001	0.999
	Forsterite	21.84	26.54	4	1.000		0.466	1.534	
	Diopside	0.13	0.16	6	1.827	0.345	0.084	0.743	1.000
	Phlogopite	0.13	0.12	11	2.968	1.064	0.095	2.873	
	Spinel	0.04	0.05	4		2.000	0.352	0.648	
Reconstructed bulk composition of CS1-Mg-silicate	Forsterite	33.23	35.22	4	1.000		0.229	1.771	
	Diopside	17.43	18.08	6	1.968	0.071	0.032	0.929	0.994
	Calcite	3.52	3.01	1				0.001	0.999
	Phlogopite	11.95	10.46	11	2.968	1.064	0.095	2.873	
	Spinel	1.31	1.54	4		2.000	0.209	0.791	
	Pargasite	32.57	31.69	23	6.002	3.009	0.128	3.863	1.998

827